A New Analysis of Eight Spitzer Phase Curves and Hot Jupiter Population Trends

Qatar-1b, Qatar-2b, WASP-52b, WASP-34b, and WASP-140b

May, E.M.; Stevenson, K.B.; Bean, J.L.; Bell, T.J.; Cowan, N.B.; Dang, L.; Desert, J.-M. ; Fortney, J.J.; Keating, D.; Kempton, E.M.-R.; Komacek, T.D.; Lewis, N.K.; Mansfield, M.; Morley, C.; Parmentier, V.; Rauscher, E.; Swain, M.R.; Zellem, R.T.; Showman, A.

DOI
10.3847/1538-3881/ac6261

Publication date
2022

Document Version
Final published version

Published in
The Astronomical Journal

The Astronomical Journal, 163:256 (18pp), 2022 June https://doi.org/10.3847/1538-3881/ac6261

A New Analysis of Eight Spitzer Phase Curves and Hot Jupiter Population Trends: Qatar-1b, Qatar-2b, WASP-52b, WASP-34b, and WASP-140b

E. M. May[1], K. B. Stevenson[1], Jacob L. Bean[2], Taylor J. Bell[3,4], Nicolas B. Cowan[3,5], Lisa Dang[3], Jean-Michel Desert[6], Jonathan J. Fortney[7], Dylan Keating[3], Eliza M.-R. Kempton[8], Thaddeus D. Komacek[8], Nikole K. Lewis[9], Megan Mansfield[10,16], Caroline Morley[11], Vivien Parmentier[12], Emily Rauscher[13], Mark R. Swain[14], Robert T. Zellem[14], and Adam Showman[15,17]

[1] Johns Hopkins APL, 11100 Johns Hopkins Road, Laurel, MD 20723, USA; Erin.May@jhuapl.edu
[2] Department of Astronomy & Astrophysics, University of Chicago, 5640 S. Ellis Avenue, Chicago, IL 60637, USA
[3] Department of Physics, McGill University, Montreal, QC, H3A 2T8, Canada
[4] BAER Institute, NASA Ames Research Center, Moffet Field, CA 94035, USA
[5] Department of Earth and Planetary Sciences, McGill University, Montreal, QC, H3A 0E8, Canada
[6] Anton Pannekoek Institute for Astronomy, University of Amsterdam, 1090 GE Amsterdam, The Netherlands
[7] Department of Astronomy & Astrophysics, University of California, Santa Cruz, CA 95064, USA
[8] Department of Astronomy, University of Maryland, College Park, MD 20742, USA
[9] Department of Astronomy and Carl Sagan Institute, Cornell University, 122 Sciences Drive, Ithaca, NY 14853, USA
[10] Steward Observatory, University of Arizona, Tucson, AZ 85719, USA
[11] Department of Astronomy, University of Texas at Austin, Austin, TX 78712, USA
[12] Department of Physics (Atmospheric, Oceanic and Planetary Physics), University of Oxford, Parks Road, Oxford, OX1 3PU, UK
[13] Department of Astronomy, University of Michigan, Ann Arbor, MI 48109, USA
[14] Jet Propulsion Laboratory (JPL), California Institute of Technology, Pasadena, CA 91109, USA
[15] Lunar and Planetary Laboratory, University of Arizona, Tucson, AZ 85721, USA
Received 2021 December 20; revised 2022 March 16; accepted 2022 March 28; published 2022 May 10

Abstract

With over 30 phase curves observed during the warm Spitzer mission, the complete data set provides a wealth of information relating to trends and three-dimensional properties of hot Jupiter atmospheres. In this work we present a comparative study of seven new Spitzer phase curves for four planets with equilibrium temperatures $T_{eq} \sim 1300$K: Qatar-2b, WASP-52b, WASP-34b, and WASP-140b, as well as a reanalysis of the 4.5 μm Qatar-1b phase curve due to the similar equilibrium temperature. In total, five 4.5 μm phase curves and three 3.6 μm phase curves are analyzed here with a uniform approach. Using these new results, in combination with literature values for the entire population of published Spitzer phase curves of hot Jupiters, we present evidence for a linear trend of increasing hotspot offset with increasing orbital period, as well as observational evidence for two classes of planets in apparent redistribution versus equilibrium temperature parameter space, and tentative evidence for a dependence of hotspot offset on planetary surface gravity in our $\sim$1300 K sample. We do not find trends in apparent heat redistribution with orbital period or gravity. Nonuniformity in literature Spitzer data analysis techniques precludes a definitive determination of the sources or lack of trends.

Unified Astronomy Thesaurus concepts: Exoplanet atmospheres (487); Exoplanet astronomy (486); Exoplanet dynamics (490); Exoplanets (498); Extrasolar gaseous planets (2172); Hot Jupiters (753)

1. Introduction

Phase curve observations are key to studying the strength and type of circulation in the atmosphere, as well as being the primary way to probe the nightside of a planet. In addition to a direct measure of the heat transport efficiency of the atmosphere, infrared phase curve observations probe transmission and emission over the course of the planet's orbit. In total, a phase curve provides the most comprehensive view of a given exoplanet's global atmospheric state. The scientific potential of phase curves does not stop at single-planet studies: observed population trends can tell us how atmospheric dynamics vary with key planetary parameters, constraining and differentiating between various atmospheric models.

The days-long orbital periods of hot Jupiters require space-based observations of their phase curves. Although multiple space telescopes exist to perform these observations, Spitzer's access to infrared wavelengths (at which planets emit thermal radiation) complements the wavelengths of optical to near-infrared observatories like the Hubble Space Telescope (HST), Kepler, and the Transiting Exoplanet Survey Satellite, which are more sensitive to reflected light.[18] This unique access to the infrared made Spitzer a popular choice for exoplanet observations—over the lifetime of the warm Spitzer mission, phase curves of over 30 planets were observed, totaling over five dozen data sets between the 3.6 and 4.5 μm channels. With notable recent exceptions (see below discussion), many analyses of these phase curve observations have been single-planet studies with individualized reduction techniques.

Spitzer InfraRed Array Camera (IRAC; Fazio et al. 2004) observations at 3.6 and 4.5 μm are primarily affected by the intrapixel-sensitivity effect, where the flux measured varies on

[16] NHFP Sagan Postdoctoral Fellow.
[17] Deceased.

[18] While the HST's Wide Field Camera 3 (WFC3) does probe emission for many hot planets, it is at different atmospheric regions than that of Spitzer.

the order of a few percent as a centroid drifts within a single pixel, or sometimes to neighboring pixels (e.g., Reach et al. 2005; Charbonneau et al. 2005; Knutson et al. 2008, 2009; Ingalls et al. 2012). Previous Spitzer analyses of exoplanet phase curves have used various methods to remove the intrapixel effect. It is these single-planet studies with nonuniform methods that limit the comparative exoplanetology possible from the entire Spitzer phase curve population. Analysis of HD 189733b and HD 209458b used a Gaussian regression of the centroid location and a noise parameter (Knutson et al. 2012; Zellem et al. 2014); pixel-level decorrelation (PLD) was used for HAT-P-7b, HD 149026b, WASP-19b, WASP-14b, and WASP-33b (Wong et al. 2015, 2016; Zhang et al. 2018); detrending via Legendre polynomials was used for WASP-18b (Maxted et al. 2013); while a form of intrapixel-sensitivity-mapping method (e.g., a Ballard map, Ballard et al. 2010; a bilinearly interpolated subpixel sensitivity, BLISS, map, Stevenson et al. 2012; or a unique method) was used for HAT-P-7b, WASP-19b, WASP-14b, WASP-43b, WASP-103b, WASP-76b, Qatar-1b, and KELT-9b (Cowan et al. 2012; Wong et al. 2015, 2016; Stevenson et al. 2017; Mendonça et al. 2018; Kreidberg et al. 2018; Bell et al. 2019; Keating et al. 2020; Mansfield et al. 2020; May & Stevenson 2020; May et al. 2021). Krick et al. (2016) used the calibration star BD+67 1044 to calibrate a sparsely sampled phase curve of WASP-14b, a similar method to our fixed-sensitivity map which we discuss below. Bell et al. (2021) presented the first uniform reanalysis of the above planets, in addition to MASCARA-1b and KELT-16b, comparing four different systematic models for all planets (BLISS mapping, PLD, polynomials, and a Gaussian process).

Bell et al. (2021) found that the BLISS-mapping method performs best for most phase curves, and in May & Stevenson (2020) we presented an update to that method at 4.5 μm to enable a more uniform approach for systematic detrending. This update applies a fixed intrapixel-sensitivity-correction map generated with Spitzer IRAC calibration data rather than the standard method of self-calibration. This minimizes differing residual systematics between data sets to enable comparative studies. Naturally, when moving to population-level studies, it is of key importance that we determine if our measured trends are astrophysical in nature or if there are unconstrained systematics in our data sets.

Numerous trends have been predicted and inferred from phase curve observations of hot Jupiters, primarily as a function of equilibrium and/or irradiation temperature.[19] Perez-Becker & Showman (2013) and Komacek & Showman (2016) explored the observational trend of increasing day–night contrast with increasing equilibrium temperature with three-dimensional models, suggesting that these trends arise due to the decreasing ratio of radiative cooling timescales to day–night wave propagation timescales. Komacek et al. (2017) took these predictions at varying atmospheric drag timescales and directly compared them to available observational data, finding models best match data at higher equilibrium temperatures—notably where more recent work suggests clouds have mostly dissipated on the nightside (see discussion of Roman et al. 2021 below, with notable caveats that Helling et al. 2019 found nightside clouds in models of WASP-18b, which has an equilibrium temperature near 2400 K). This dependence of temperature on phase amplitude is also discussed in Kataria et al. (2016).

Zhang et al. (2018) saw evidence in published data for a decrease in hotspot offset with increasing irradiation temperature, with an inflection point and increasing offsets after 3500 K; however this disagrees with some three-dimensional model predictions such as those of Perna et al. (2012), Kataria et al. (2016), Komacek et al. (2017), Zhang & Showman (2017), and Parmentier et al. (2021). In fact, Kataria et al. (2016) predicted the opposite: that the infrared phase offset will be smaller for the hottest planets that they modeled. Observational results from Beatty et al. (2019) and Keating et al. (2019) also disagree with this offset trend while also suggesting that the nightsides of all hot Jupiters are all roughly 1000 K due to clouds. Bell et al. (2021) similarly present little evidence for a trend between hotspot offset and temperature in the observed sample, but see evidence for the same increase in day–night contrast with temperature as previously seen in observations and predicted by models.

More recent modeling by Roman et al. (2021) looks at bolometric phase-dependent emission and predicts a dissipation of most nightside clouds near an equilibrium temperature of 2000 K, with cloudy and clear phase curves converging past this point. For clear atmospheres, they predict a decrease of hotspot offset and an increase in amplitude with increasing temperature. Exact trends for their cloudy models depend on the assumptions made, with general peaks in phase offset around $T_{\rm eq} \sim 2000$ K while amplitudes decrease then flatten off around the same temperature. Parmentier et al. (2021), expanding on the work of Parmentier et al. (2016), did not extend their models past $T_{\rm eq} \sim 2000$ K, primarily focusing on the differences between clear and cloudy cases. Their clear models broadly agree with Roman et al. (2021) while the shape and inflection points of their relationships between offset/amplitude and equilibrium temperature in their cloudy models depends on the assumed cloud composition and particle size. Parmentier et al. (2021) also present model predictions for the apparent redistribution factor ($T_b^4/T_{\rm eq}^4$, where T_b refers to brightness temperature and $T_{\rm eq}$ the equilibrium temperature) in the Spitzer band passes, for both cloudy and cloud-free general circulation models, as a function of equilibrium temperature from 1000 to 2000 K.

In this work, we take steps toward completing the analysis of the remaining unpublished Spitzer phase curves and present results for seven new Spitzer phase curves from four planets, Qatar-2b, WASP-52b, WASP-34b, and WASP-140b, as well as a reanalysis of the 4.5 μm Qatar-1b phase curve using our fixed intrapixel-sensitivity map. Five of these phase curves were observed at 4.5 μm and three at 3.6 μm. We present as uniform of a data reduction as possible, with a consistent use of systematic models (standard BLISS or fixed BLISS maps) throughout. Standard BLISS and fixed BLISS maps generally agree within uncertainties, but the use of the fixed BLISS map when appropriate eliminates other degeneracies between the astrophysical and systematic signals. While we do not apply the exact same systematic method to each data set, the analysis is performed by a single person applying the same criteria, which results in a more uniform reduction than has generally been done in the current literature (notable exceptions include Bell et al. 2021, which takes a uniform analysis approach). Keating et al. (2020) adopted a similar approach to study trends for a set of three planets with equilibrium temperature ~1400 K planets.

[19] The irradiation temperature is related to the equilibrium temperature as $T_{\rm irr} = \sqrt{2}\,T_{\rm eq}$.

Table 1
Observational Details

Label	Observation Date	Duration (hrs)	Frame. Time (s)	Total Frames	Band (μm)
qa001bo21	May 02-03 2018	39.6	2.0	70,464	4.5
qa002bo11	May 29-31 2017	38.2	2.0	67,904	3.6
qa002bo21	May 21-23 2017	38.2	2.0	67,904	4.5
wa052bo11	Oct 17-19 2016	48.3	2.0	85,824	3.6
wa052bo12	Oct 21-23 2017	47.9	2.0	85,248	3.6
wa052bo21	Oct 21-23 2018	47.9	2.0	85,248	4.5
wa034bo11	Nov 03-08 2020	112.4	2.0	191,424	4.5
wa140bo11	Jan 01-04 2019	59.5	2.0	105,728	4.5

Note. Label denotes the planet (e.g., qa001b=Qatar-1b), type of observation (o=orbit), Spitzer IRAC channel (1 or 2), and visit number (1 or 2).

This uniform approach better enables population-level trends, which we examine at the end of this paper (similar large, uniform analyses to enable population studies have been done on Spitzer eclipses and transits, e.g., Baxter et al. 2021 and Mansfield et al. 2021). All five planets in our sample have similar equilibrium temperatures near 1300 K, allowing us to specifically focus on trends in secondary parameters such as orbital period and gravity. Theory predicts that the circulation and heat redistribution of tidally locked hot Jupiter atmospheres is governed by nondimensional parameters that depend on, among other things, rotation rate (directly related to orbital period for tidally locked hot Jupiters, which is assumed here) and gravity—suggesting that trends in phase curve parameters due to secondary parameters are expected. For example, the ratio between the wave propagation timescale and radiative timescale governs the day–night heat transport, and therefore determines the phase curve amplitude (Perez-Becker & Showman 2013; Komacek & Showman 2016). This temperature range also results in a more direct comparison to model predictions because it is below the threshold where one needs to consider the effects of magnetohydrodynamics (MHD) and hydrogen dissociation, commonly not included in three-dimensional models.

In Section 2 we introduce each planet and an overview of the observations of their respective data sets. Section 3 discusses the data-reduction techniques, including systematic and astrophysical models. Section 4 presents our phase curve results, with comparisons between planets discussed in Section 5. Conclusions of this work are discussed in Section 6. Files containing phase curve data, model fits, and parameters used in our population studies are available online.[20]

2. Spitzer Observations

Here we discuss the data sets used in this work. Table 1 provides an overview of the relevant data sets and Table 2 provides an overview of the relevant planetary parameters. All phase curves were observed by Spitzer's IRAC (Fazio et al. 2004). As is standard, each phase curve starts before a secondary eclipse event and contains two secondary eclipse events and one transit event. Containing two eclipses allows for two points of reference that help minimize degeneracies between visit-long systematic and astrophysical trends. Figure 1 shows the changes in x- and y-centroids over the course of all phase curve observations, as well as the corresponding raw flux.

2.1. Qatar-1b

One phase curve each at 3.6 μm and 4.5 μm were obtained as part of program 13038 (PI: Kevin Stevenson). Qatar-1b is a $1.294^{+0.052}_{-0.029}$ $M_{\rm Jup}$, $1.143^{+0.026}_{-0.025}$ $R_{\rm Jup}$ planet with an equilibrium temperature 1360 ± 28 K (using the most recent complete set of parameters from Collins et al. 2017) and was first identified by Alsubai et al. (2011). The phase curves from this program were previously analyzed and reported by Keating et al. (2020) and Bell et al. (2021); here, we reanalyze the 4.5 μm observation using the uniform Spitzer sensitivity map at 4.5 μm presented in May & Stevenson (2020). Spitzer eclipses of Qatar-1b (one each at 3.6 and 4.5 μm) were analyzed by Garhart et al. (2018) and included in a statistical analysis of secondary eclipses by Garhart et al. (2020).

2.2. Qatar-2b

One phase curve each at 3.6 μm and 4.5 μm of Qatar-2b were obtained as part of program 13038 (PI: Kevin Stevenson). Qatar-2b is a 2.487 ± 0.086 $M_{\rm Jup}$, 1.144 ± 0.035 $R_{\rm Jup}$ planet with an equilibrium temperature 1290 ± 14 K (using the most recent complete set of parameters from Močnik et al. 2017). The discovery of Qatar-2b was reported by Bryan et al. (2012).

2.3. WASP-52b

Two 3.6 μm and one 4.5 μm phase curves of WASP-52b were observed as a part of program 13038 (PI: Kevin Stevenson). WASP-52b is a 0.46 ± 0.02 $M_{\rm Jup}$, 1.27 ± 0.03 $R_{\rm Jup}$ planet with an equilibrium temperature 1300 ± 35 K (using the most recent complete set of parameters from Öztürk & Erdem 2019). WASP-52b was first identified by Hébrard et al. (2013). The transits from the first 3.6 μm visit and the single 4.5 μm visit were reduced and reported by Alam et al. (2018).

2.4. WASP-34b

One 4.5 μm phase curve of WASP-34b was observed as part of program 14059 (PI: Jacob Bean). With an orbital period of 4.317 days, this was the longest Spitzer phase curve of a standard hot Jupiter observed during the telescope's lifetime (HAT-P-2b, while on a longer orbit, is eccentric and not used in our comparison studies). WASP-34b is a 0.59 ± 0.01 $M_{\rm Jup}$, $1.22^{0.11}_{-0.08}$ $R_{\rm Jup}$ planet with an equilibrium temperature 1158 ± 30 K (using the most recent complete set of parameters from the discovery paper; Smalley et al. 2011). Notably, WASP-34b has a grazing transit and eclipse, with an impact parameter of $0.904^{+0.017}_{-0.014}$.

2.5. WASP-140b

One 4.5 μm phase curve of WASP-140b was observed as part of program 14059 (PI: Jacob Bean). WASP-140b is a 2.44 ± 0.07 $M_{\rm Jup}$, $1.44^{+0.42}_{-0.18}$ $R_{\rm Jup}$ planet with an equilibrium temperature 1320 K (Hellier et al. 2017). WASP-140b is the only eccentric planet in this study, with an eccentricity of 0.0470 ± 0.0035. The star likely is relatively young, at 0.42 ± 0.06 Gyr (Hellier et al. 2017), based on a 10.4 rotational

[20] https://www.github.com/erinmmay/Spitzer_Uniform_Phase_Curves

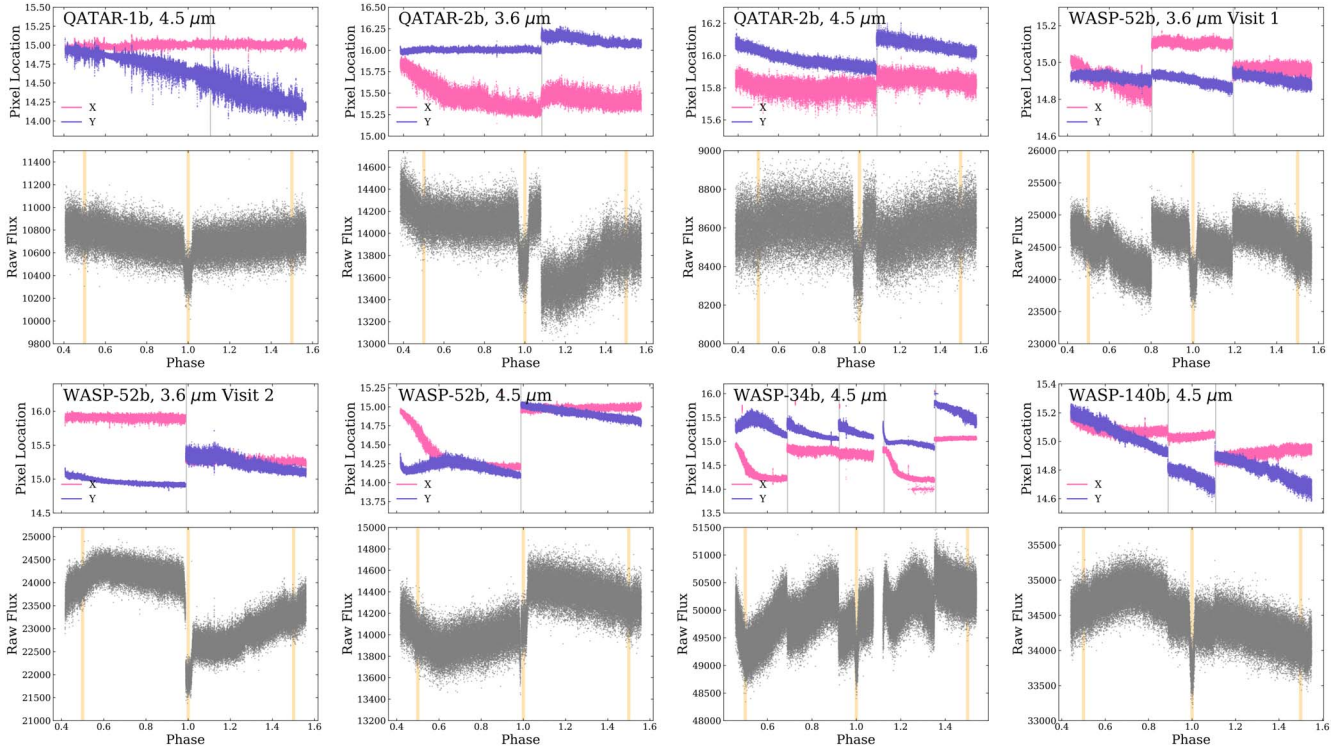

Figure 1. *X*- and *y*-centroids (top) and corresponding raw (uncorrected) flux (bottom) for all phase curves analyzed in this study. In the top panel, the Astronomical Observation Request (AOR) gaps are marked and in the bottom panel phases of ±0.5 and 1.0 are marked to guide the eye. Full-size versions of each image are available on our Uniform Phase Curve Repository.

Table 2
Planet Parameters

Planet	a (AU)	log(g) (cm/s^2)	Radius (R_{Jup})	Mass (M_{Jup})	T_{eq} (K)	Period (days)	Reference
Qatar-1b	0.0233 ± 0.0040	3.390 ± 0.015	$1.143^{+0.026}_{-0.025}$	$1.294^{+0.052}_{-0.049}$	1360 ± 28	$1.42002420 \pm 2.2E\text{-}7$	Collins et al. (2017)
Qatar-2b	0.02149 ± 0.00036	3.638 ± 0.022	1.144 ± 0.035	2.487 ± 0.086	1290 ± 14	$1.3371182 \pm 3.7E\text{-}6$	Bryan et al. (2012)
WASP-52b	0.0272 ± 0.003	2.81 ± 0.03	1.27 ± 0.03	0.46 ± 0.02	1300 ± 35	$1.7497798 \pm 1.2E\text{-}6$	Hébrard et al. (2013)
WASP-34b	0.0524 ± 0.0004	$2.96^{+0.05}_{-0.07}$	$1.22^{+0.11}_{-0.08}$	0.59 ± 0.01	1158 ± 30	$4.3176782 \pm 4.5E\text{-}6$	Smalley et al. (2011)
WASP-140b	0.0323 ± 0.0005	3.4 ± 0.2	$1.44^{+0.42}_{-0.18}$	2.44 ± 0.07	1317 ± 40	$2.2359835 \pm 8E\text{-}7$	Hellier et al. (2017)

Note. Equilibrium temperatures are calculated from values in this table and Table 3.

period and ages from Barnes (2007), which, compared to the circularization timescale of the orbit, suggests that WASP-140b only recently arrived at its present location. Although WASP-140b does have the same equilibrium temperature as the rest in this sample, the eccentricity puts WASP-140b in a category on its own. Regardless, we include the analysis here for completeness.

3. Data Reduction and Analysis

3.1. Initial Data Reduction

Data reduction and analysis is done with the Photometry for Orbits, Eclipses, and Transits (POET; Campo et al. 2011; Stevenson et al. 2012; Cubillos et al. 2013) pipeline, including recent updates from May & Stevenson (2020) to improve systematic modeling at 4.5 μm by applying a fixed-sensitivity map rather than self-calibrating. We use two-dimensional Gaussian centroiding following the suggestions of Lust et al. (2014). All data sets are extracted using a fixed aperture size optimized for the standard deviation of the normalized residuals (SDNR). To determine the best aperture, we extract apertures between 2.0 and 4.0 pixels in 0.25 pixel increments. For all data sets we use a fixed annulus between 7 and 15 pixels away from the centroids for background subtractions. The best aperture size for each data set is included in Table 4.

3.1.1. The Intrapixel-sensitivity Effect

The dominant sources of Spitzer IRAC systematics at 3.6 and 4.5 μm are intrapixel-sensitivity variations as the centroid drifts within a single pixel. We use BLISS mapping (Stevenson et al. 2012) to model and remove this effect. In May & Stevenson (2020) we showed that BLISS mapping is degenerate with point response function (PRF) at FWHM detrending. PRF-FWHM detrending is a second-level detrending function that accounts for the shape of the PRF stretching

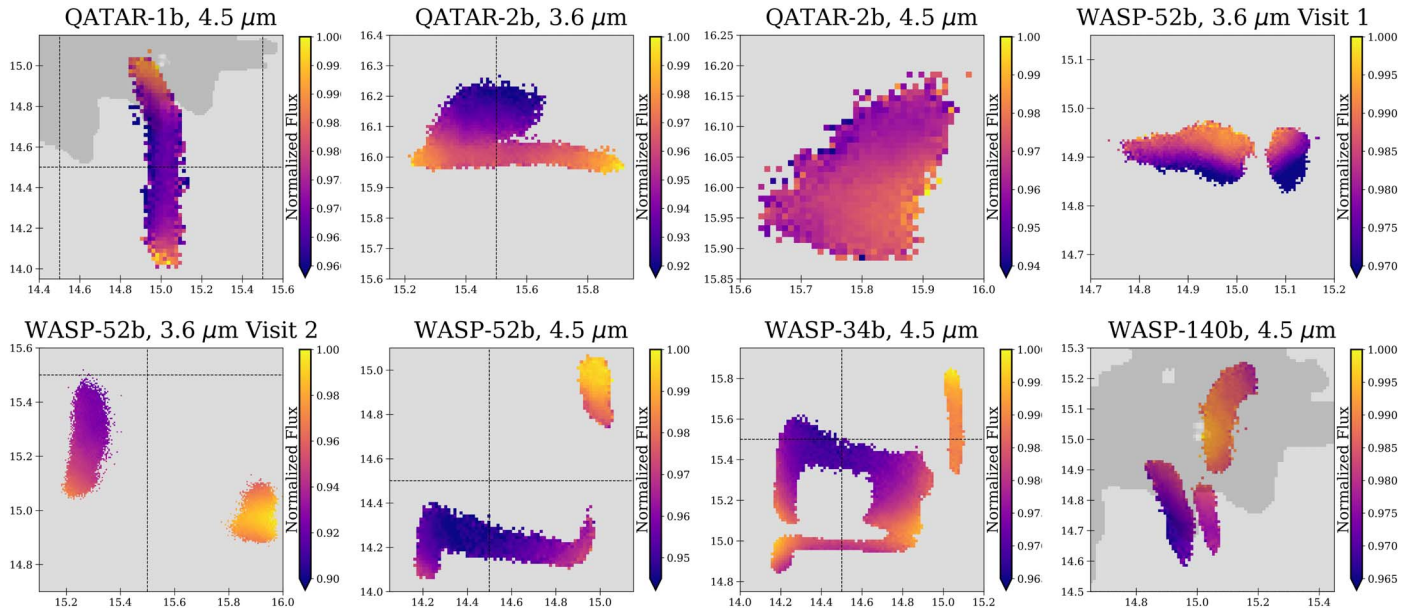

Figure 2. BLISS maps for the data sets analyzed in this work. The color bar denotes the relative sensitivity of a given subpixel element. The 4.5 μm observations also show the extent of our fixed-sensitivity map in the dark shaded region. The dashed lines denote the edges of a pixel (where relevant), with axis labels in subpixel units. Full-size versions of each image are available on our Uniform Phase Curve Repository.

toward an oval for centroids near the edges of the pixel (see Section 3.1.2). When temporally binning the data, this degeneracy becomes stronger due to smoothing over the features that allow one to fit the two methods independently. Therefore, we do not perform any temporal binning on any of the data sets presented in this work.

For the 4.5 μm data sets that fully or partially overlap with our fixed intrapixel-sensitivity map, our systematic model uses the overlapping regions to detrend the data, and self-calibrates using standard BLISS mapping in nonoverlapping regions. The transition from self-calibration to fixed-map calibaration is smooth, with no artifacts. For the remaining 4.5 μm data sets that do not at least partially overlap with our fixed-sensitivity map, the data sets fully self-calibrate using standard BLISS mapping. As discussed in May & Stevenson (2020), 3.6 μm sensitivity is time variable and a fixed-sensitivity map cannot be generated. As a result, all 3.6 μm data sets are self-calibrated with standard BLISS mapping. Figure 2 shows the best fit BLISS maps for all data sets in this study.

The standard BLISS map is described by the intrapixel spatial binning size and the minimum number of exposures required for a given spatial bin to be used in the fit. To determine the best set of these parameters, we compare model fits to a nearest-neighbor approach and identify the step size that produces the best Bayesian information criterion (BIC) and SDNR, respectively, without overfitting the data. See Stevenson et al. (2012) for more details on our methods.

3.1.2. Point Response Function Detrending

The IRAC PRF tends to stretch toward an oval rather than a circle as a centroid drifts toward the edge of a pixel. Because we use circular apertures, this can result in flux being undercounted. Previous works have used a method to correct this by detrending against the Gaussian widths of the PRF with varying polynomial orders (Knutson et al. 2012; Lewis et al. 2013; Lanotte et al. 2014; Demory et al. 2016b, 2016a; Gillon et al. 2017; Mendonça et al. 2018), given as

$$f = x_1(s_x - s_0) + x_2(s_x - s_0)^2 + x_3(s_x - s_0)^3 + y_1(s_y - s_0) + y_2(s_y - s_0)^2 + y_3(s_y - s_0)^3 + c, \quad (1)$$

where s_x and s_y are the x- and y-dimension Gaussian width in pixels, s_0 is an offset (typically 0.5 pixels), $x_{\{1,2,3\}}$ and $y_{\{1,2,3\}}$ are the polynomial coefficients, and c is a constant.

We test applying the PRF detrending when a free (i.e., standard) BLISS map is used, comparing 1st-, 2nd-, and 3rd-order polynomials and selecting for the lowest BIC. The fixed-sensitivity map encapsulates the loss of flux from changing PRF shape, and does not require this step. In general, most of our data sets with the free map do prefer the addition of the PRF detrending with one exception; see Table 4.

3.1.3. Astrophysical Source Models

We adopt a generic sinusoidal function to model each planet's emission considering both a full-period and half-period component (Cowan & Agol 2008 find that a sinusoid is the best model for fitting full phase curves). The addition of a half-period sinusoidal function results in asymmetric phase curves. We use the `BATMAN` package to model the transit events (Kreidberg 2015) with eclipses modeled using a form of the analytic method presented by Mandel & Agol (2002), with the exception of WASP-34b, which is a grazing event. For the WASP-34b eclipses we used `BATMAN`, which includes an impact parameter input. All transits are modeled assuming quadratic limb darkening based on interpolated Kurucz stellar models (Castelli & Kurucz 2003) using `ExoCTK`'s limb-darkening tool (Bourque et al. 2021). Table 3 gives an overview of the stellar parameters and limb-darkening coefficients adopted for each host star.

We further consider the presence of temporal ramps; including no ramp and linear ramps, as well as quadratic or exponential ramp models for select data sets. The best-fit combination of the systematic model, temporal ramp, and

Table 3
Stellar Parameters and Limb Darkening

Star	$T_{\rm eff}$ (K)	log(g) (cm/s^2)	[Fe/H] (dex)	Ch. (μm)	C_1	C_2
Qatar-1	5013^{+93}_{-88}	$4.552^{+0.012}_{-0.011}$	$0.17^{+0.097}_{-0.094}$	4.5	0.100	0.110
Qatar-2	4654 ± 50	4.601 ± 0.018	0.02 ± 0.08	3.6	0.116	0.166
				4.5	0.107	0.120
WASP-52	5000 ± 100	4.582 ± 0.014	0.03 ± 0.12	3.6	0.108	0.147
				4.5	0.100	0.107
WASP-34	5700 ± 100	4.50 ± 0.10	0.040 ± 0.100[a]	4.5	0.090	0.099
WASP-140	5260 ± 100	4.51 ± 0.04	0.12 ± 0.10	4.5	0.095	0.105

Notes. C_1 and C_2 are the quadratic limb-darkening parameters. Unless otherwise noted, stellar parameters are from the same source as the planetary parameters in Table 2.
[a] WASP-34b metallicity from Stassun et al. (2019).

astrophysical sources is identified using the BIC (Liddle 2007), with the exception of model combinations that produce significantly nonphysical events (i.e., relative flux ratios less than 1.0 for nongrazing events). We compute the best-fit models using a Levenberg–Marquardt minimizer, and our parameter uncertainties are estimated using a custom differential-evolution Markov Chain algorithm (DEMC; ter Braak & Vrugt 2008). In Table 4 we present the ΔBIC comparison of our various model combinations for all phase curves. The combination with the best BIC for each observation (shown as the bolded row) is identified as our "best-fit" model. In several cases the use of a quadratic ramp results in a nightside flux ratio less than 1.0, which we discard as nonphysical. See Section Appendix for details about which paramters are fit and which are held constant. Each parameter takes a bounded uniform prior (e.g., time parameters are bounded based on the start and end times of the entire data set).

In the following sections we discuss the results for each phase curve.

4. Results

In the following sections we detail the individual results for each target, with final best-fit values presented in Table 5.

4.1. Qatar-1b

Because the centroids of Qatar-1b fall only partially on the master map (see Figure 1), we reduce the Qatar-1b 4.5 μm phase curve using both our fixed-map method and the standard BLISS-map method to compare the resulting phase curves. Recall that partial overlap uses self-calibration in nonoverlapping regions, but that the overlapping regions provide constraints, particularly when one eclipse overlaps, as is the case here.

Figure 3 shows our best fit(s): the top panel compares our fit with the free map (dashed pink line, standard BLISS method), and fixed map (solid black line) compared to 200 random draws of the free-map fit to demonstrate that the resulting phase functions are generally consistent. The middle panel shows the best fixed-map fit compared to the binned data (data is fit without binning but plotted using bins for ease of presentation). The bottom panel shows the residuals. For this figure, and all following phase curve figures, the vertical shaded region shows the measured offset and associated 1σ uncertainties, while the horizontal shaded region denotes the 1σ uncertainty on the phase curve minimum.

For Qatar-1b at 4.5 μm, we measure a nightside band-integrated brightness temperature 1098 ± 158 K and a dayside band-integrated temperature 1696 ± 39 K. Full results including amplitude, fluxes, offset, eclipse and transit depths are reported in Table 5.

Both the 4.5 μm Qatar-1b phase curve and a 3.6 μm phase curve that we do not refit were first analyzed by Keating et al. (2020). The middle panel of Figure 3 compares our best fit to that of Keating et al. (2020). Both our phase-amplitude (calculated based on fluxes) and hotspot offset values agree to within 1σ with a similar slight westward offset as identified by Keating et al. (2020). However, the dayside temperature between our two works is discrepant by 3σ. This larger difference in temperatures compared to the general agreement between the phase function and eclipse depths is likely a result of the different stellar parameters used to estimate the wavelength-integrated stellar flux in these channels.

4.2. Qatar-2b

For both Qatar-2b data sets, we use the standard BLISS-mapping method to remove the intrapixel sensitivity. We also consider 1st-, 2nd-, and 3rd-order PRF functions for further detrending and find that 2nd order performs best for both channels.

4.2.1. 3.6 μm

In our initial analysis of the 3.6 μm data set we identify a high-frequency sinusoidal systematic. While this may be due to instrumental reasons, we also note that Qatar-2b has been identified as an active star featuring recurring star spots (e.g., Mancini et al. 2014; Močnik et al. 2017), and, as such, we cannot discount stellar activity. Either way, we chose to model this as an additional source of correlated noise, applying the wavelet methodology of Carter & Winn (2009). This allows us to encapsulate the uncertainty introduced by this high-frequency signal into the errors on our reported parameters.

Figure 4 shows our best fit to this data set compared to 200 random draws of the DEMC run. For Qatar-2b at 3.6 μm, we measure a nightside band-integrated brightness temperature 842 ± 141 K and a dayside band-integrated brightness

temperature 1421 ± 28 K. Full results including amplitude, fluxes, offset, eclipse and transit depths are reported in Table 5.

4.2.2. 4.5 μm

The centroids for Qatar-2b do not overlap with our fixed-sensitivity map, so we chose to use the standard free BLISS-map approach.

As denoted in Table 4, simple ΔBIC comparisons would suggest that an asymmetric phase function with a quadratic ramp performs best. However, this fit, and the linear ramp option with either a symmetric or asymmetric phase function, result in negative nightside flux, which is an unphysical result. We therefore consider the symmetric + quadratic ramp as the best fit. We note that all of these model combinations resulted in the same phase offset and the symmetric best-fit amplitudes are within 1σ. The top panel of Figure 5 shows a comparison of these four model combinations and 200 random draws of our best-fit model (solid black line). The general shape of the symmetric + linear combination is relatively similar to that of the quadratic ramp, but the asymmetric functions clearly diverge, which we discuss below.

Further, as shown in Figure 5, there is an undetermined systematic after transit that appears in both channels near the jump in centroids at the AOR gap (phase of ∼1.1–1.2). By eye, it is clear that these asymmetric models are attempting to fit this systematic, providing further weight to our decision to not consider those models. We also find that clipping this region leads to a worse constraint on the BLISS map for this event, with slight modifications in the clipped region heavily impacting the measured phase offset and amplitude. For this reason, and the above discussion, we make the decision not to clip this region.

As also identified in the 3.6 μm data for this target, we find a present, though weaker, high-frequency sinusoidal systematic. We follow the same approach as at 3.6 μm to ensure that our errors encapsulate this uncertainty. The middle panel of Figure 5 shows our best fit.

For Qatar-2b at 4.5 μm we measure a nightside band-integrated brightness temperature 724 ± 135 K and a dayside band-integrated brightness temperature 1368 ± 32 K. Full results including amplitude, fluxes, offset, eclipse and transit depths are reported in Table 5.

4.3. WASP-52b

4.3.1. 3.6 μm

Two phase curves of WASP-52b were observed at 3.6 μm. As shown in Figure 2, both observations have two nonoverlapping groups of centroids, which makes removing the intrapixel effect particularly difficult. We found that, individually, the phase curve parameters were poorly constrained due to a degeneracy between the pixel-position and phase-function parameters. To mitigate this as best as possible, we performed a joint fit of both visits with all astrophysical signal parameters tied to each other between visits, while the systematics were individually fit to account for time variability in the 3.6 μm intrapixel response (3.6 μm sensitivity variability is discussed in May & Stevenson 2020). In Table 4 we include the ΔBICs for both events from a given joint fit. Because of the unphysical negative nightside flux resulting from the use of a quadratic ramp, we select the linear temporal ramp with a symmetric phase function as our best fit. Figure 6 shows our best-fit phase function compared to both data sets as well as 200 random draws from our Markov Chain Monte Carlo (MCMC) chains.

For WASP-52b at 3.6 μm we measure a nightside band-integrated brightness temperature 1116 ± 46 K and a dayside

Table 4
Best-fit Models

Label	Aperture [Pixels]	Systematic Model	Ramp Model	Phase Model	ΔBIC
qa001bo21	2.25	Fixed	⋯	Symm.	108.4
		BLISS	Lin.	Symm.	5.9
			Quad.	**Symm.**	**0.0**
			⋯	Asymm.	130.6
			Lin.	Asymm.	28.2
			Quad.	Asymm.	20.4
qa002bo11	2.00	Free	⋯	Symm.	40.6
		BLISS	Lin.	Symm.	5.4
		+	**Quad.**	**Symm.**	**0.0**
		2nd	⋯	Asymm.	59.6
		order	Lin.	Asymm.	27.6
		PRF	Quad.	Asymm.	13.0
qa002bo21	2.25	Free	⋯	Symm.	96.6
		BLISS	Lin.	Symm.	⋯
		+	**Quad.**	**Symm.**	**0**
		2nd	⋯	Asymm.	95.3
		order	Lin.	Asymm.	⋯
		PRF	Quad.	Asymm.	⋯
wa052bo11	2.25	Free	⋯	Symm.	1810.2
		BLISS	**Lin.**	**Symm.**	**0.0**
		+	Quad.	Symm.	⋯
		2nd	⋯	Asymm.	1773.4
		order	Lin.	Asymm.	134.1
		PRF	Quad.	Asymm.	⋯
wa052bo12	2.25	Free	⋯	Symm.	533.6
		BLISS	**Lin.**	**Symm.**	**0.0**
		+	Quad.	Symm.	⋯
		2nd	⋯	Asymm.	1442.1
		order	Lin.	Asymm.	740.0
		PRF	Quad.	Asymm.	674.2
wa052bo21	2.25	Free	⋯	**Symm.**	**0.0**
		BLISS	Lin.	Symm.	10.6
		+	Quad.	Symm.	21.6
		2nd	⋯	Asymm.	22.5
		order	Lin.	Asymm.	33.1
		PRF	Quad.	Asymm.	44.1
wa034bo11	2.75	Free	⋯	**Symm.**	**0.0**
		BLISS	2 Lin.	Symm.	24.0
			2 Exp./Lin.	Symm.	57.6
			⋯	Asymm.	115.1
			2 Lin.	Asymm.	58.3
			2 Exp./Lin	Asymm.	80.0
wa140bo11	2.50	Fixed	⋯	Symm.	6.2
		BLISS	Lin.	Symm.	6.5
			Quad.	Symm.	16.4
			⋯	**Asymm.**	**0.0**
			Lin.	Asymm.	7.7
			Quad.	Asymm.	14.9

Notes. Lin. = linear temporal ramp; Quad. = quadratic temporal ramp. Some model combinations result in significantly nonphysical best fits (i.e., negative nightside flux or phase offsets >90°). For further explanation, see text for that planet. Bolded rows denote the best fit.

Table 5
Fit Results

		qa001bo21	qa002bo11	qa002bo21	wa052bo11 / wa052bo12	wa052bo21	wa034bo21*	wa140bo21
Eclipse depth	[ppm]	2914 ± 162	2223 ± 118	3004 ± 185	2201 ± 77	3350 ± 162	850 ± 95	2022 ± 111
Transit depth	[R_p/R_S]	0.14514 ± 0.00018	0.16369 ± 0.00011	0.16189 ± 0.00015	0.16464 ± 0.00011	0.16305 ± 0.00014	0.12007 ± 0.0002	0.17399 ± 0.00012
Hotspot offset	[$^{\circ}$]	-7.98 ± 5.79	0.6 ± 5.8	-5.2 ± 5.4	-2.1 ± 4.9	31.8 ± 7.8	34.7 ± 4.7	-55.7 ± 28.3
Amplitude	[ppm]	769 ± 213	1039 ± 165	1442 ± 221	650 ± 79	812 ± 204	446 ± 78	624 ± 80
F_p/F_s [ppm]	Max	2930 ± 164	2228 ± 119	3019 ± 193	2207 ± 77	3483 ± 181	930 ± 97	2302 ± 111
	Min	1392 ± 394	151 ± 308	136 ± 399	906 ± 138	1860 ± 366	38 ± 122	1053 ± 114
	Day	2922 ± 163	2227 ± 118	3018 ± 186	2206 ± 77	3365 ± 163	851 ± 95	1904 ± 111
	Night	1399 ± 213	152 ± 309	138 ± 400	906 ± 138	1978 ± 357	117 ± 123	2064 ± 132
Temperature [K]	Max	1697 ± 39	1422 ± 28	1370 ± 33	1455 ± 21	1504 ± 36	1222 ± 47	1252 ± 25
	Min	1096 ± 157	840 ± 141	720 ± 134	1115 ± 45	1195 ± 81	666 ± 117	973 ± 32
	Day	1696 ± 39	1421 ± 28	1368 ± 32	1454 ± 21	1481 ± 34	1185 ± 47	1169 ± 25
	Night	1098 ± 158	842 ± 141	724 ± 135	1116 ± 46	1224 ± 77	726 ± 119	1201 ± 29

Note. Label denotes the planet (e.g., qa001b = Qatar-1b), type of observation (o = orbit), Spitzer IRAC channel (1 or 2), and visit number (1 or 2). "Max" and "Min" refer to the maximum and minimum of the phase curve. "Day" and "Night" refer to a phase of 0.0/1.0 and 0.5, respectively. A positive phase offset corresponds to an eastward shift. Amplitude is given as (max-min)/2.

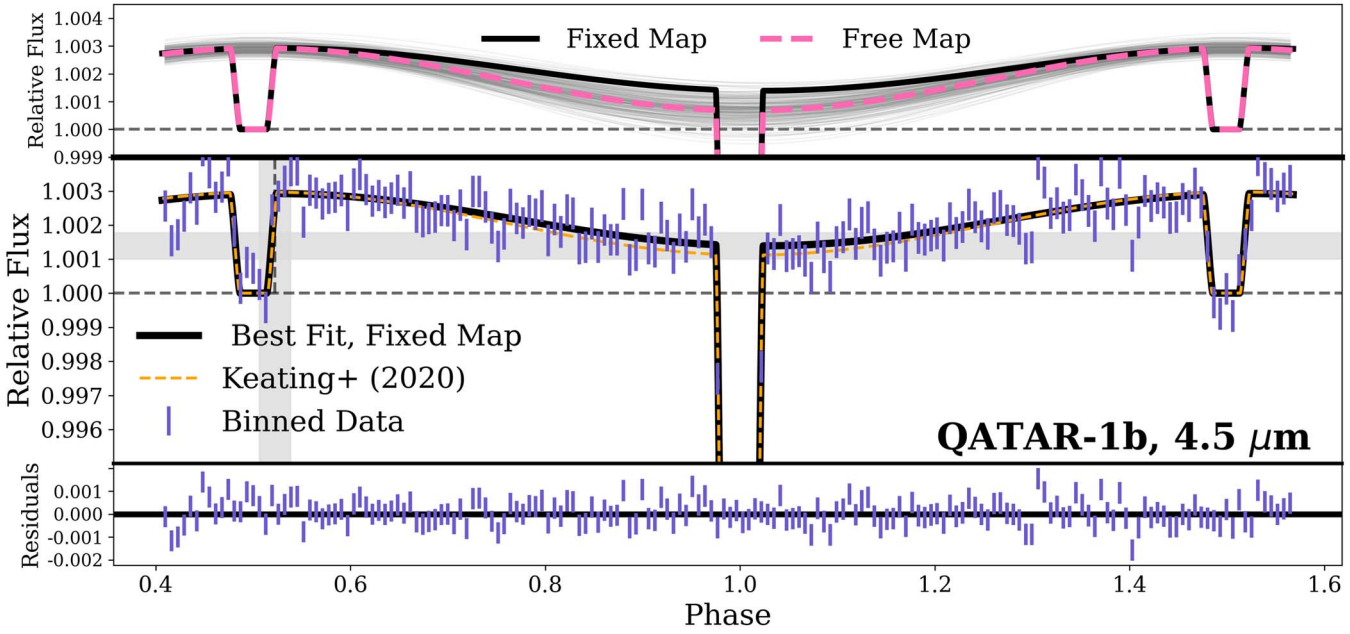

Figure 3. Qatar-1b 4.5 μm phase curve best fits. Top: a comparison between the fixed and standard (free) BLISS-mapping methods, compared to 200 random draws of the free-map fit (note, the fixed map only partially overlaps with the centroids). Middle: best-fit fixed map compared to the binned data. The horizontal shaded regions corresponds to the uncertainty on the minimum flux while the vertical region corresponds to the uncertainty on the phase offset. Bottom: the residuals. Our results agree well with those from Keating et al. (2020).

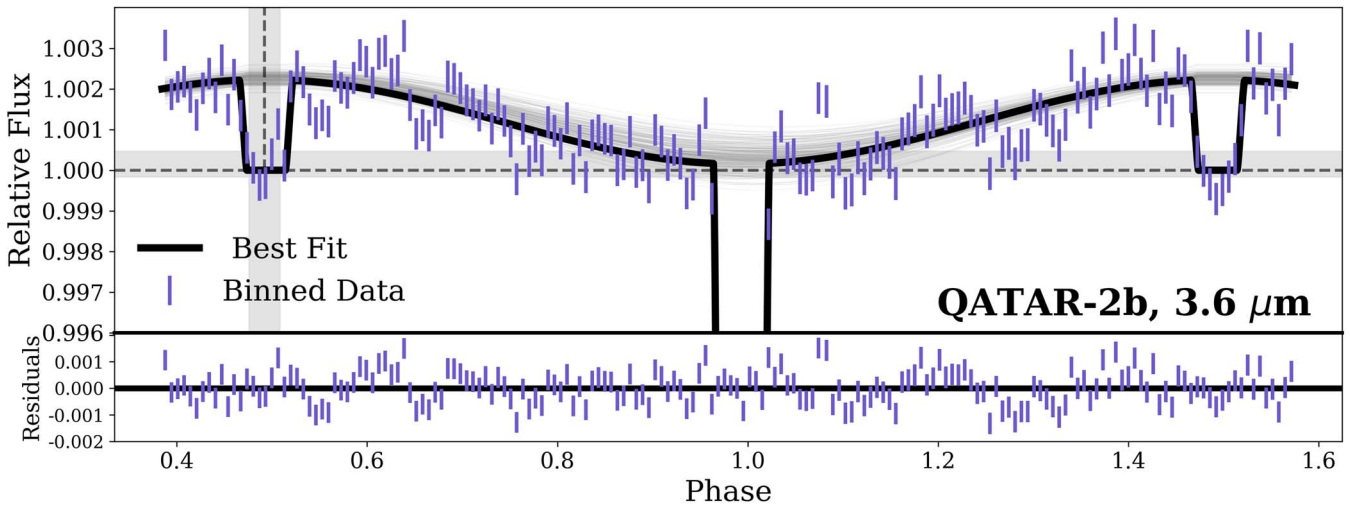

Figure 4. Qatar-2b 3.6 μm phase curve best fits. Top: best model combination (Symm. + Quad.) compared to 200 random draws of the best fit, shown as lightly shaded lines. Binned data are overplotted. The horizontal shaded regions correspond to the uncertainty on the minimum flux while the vertical region corresponds to the uncertainty on the phase offset Bottom: the residuals.

band-integrated brightness temperature 1454 ± 21 K. Full results including amplitude, fluxes, offset, eclipse and transit depths are reported in Table 5.

4.3.2. 4.5 μm

The 4.5 μm phase curve of WASP-52b partially overlaps with our fixed-sensitivity map. For this data set, the long swipe of centroids centered at a y-position of $\sim$14.2 represent centroids that are never revisited, leaving a strong degeneracy between astrophysical and systematic signals (when centroids slowly drift and do not remain fairly constant, the change in flux due to changing centroids can mimic visit-long trends like the planet's phase curve). Because of this and a larger than normal effect of the PRF Gaussian widths, we find that this data set is not well modeled by the fixed-sensitivity map. As a result, we use a standard BLISS-map approach and find that a 2nd-order PRF-FWHM produces the best results. Our best fit adopts no temporal ramp with a symmetric phase function.

The top panel of Figure 7 shows our best-fit free map (solid black line) compared to our best-fit fixed map (dashed pink) and 200 draws of the best free-map fit. When using the fixed map, we find that this degeneracy between the intrapixel sensitivity and phase function results in the phase curve offset being strongly dependent on the choice of temporal ramp. Notably, a linear ramp results in an inverted phase curve (i.e., a phase offset of 180°, suggesting the nightside is the hottest, an unphysical result) while a quadratic ramp results in a phase offset of 75°, also a result that is unexpected from three-dimensional models, which predict significantly smaller offsets.

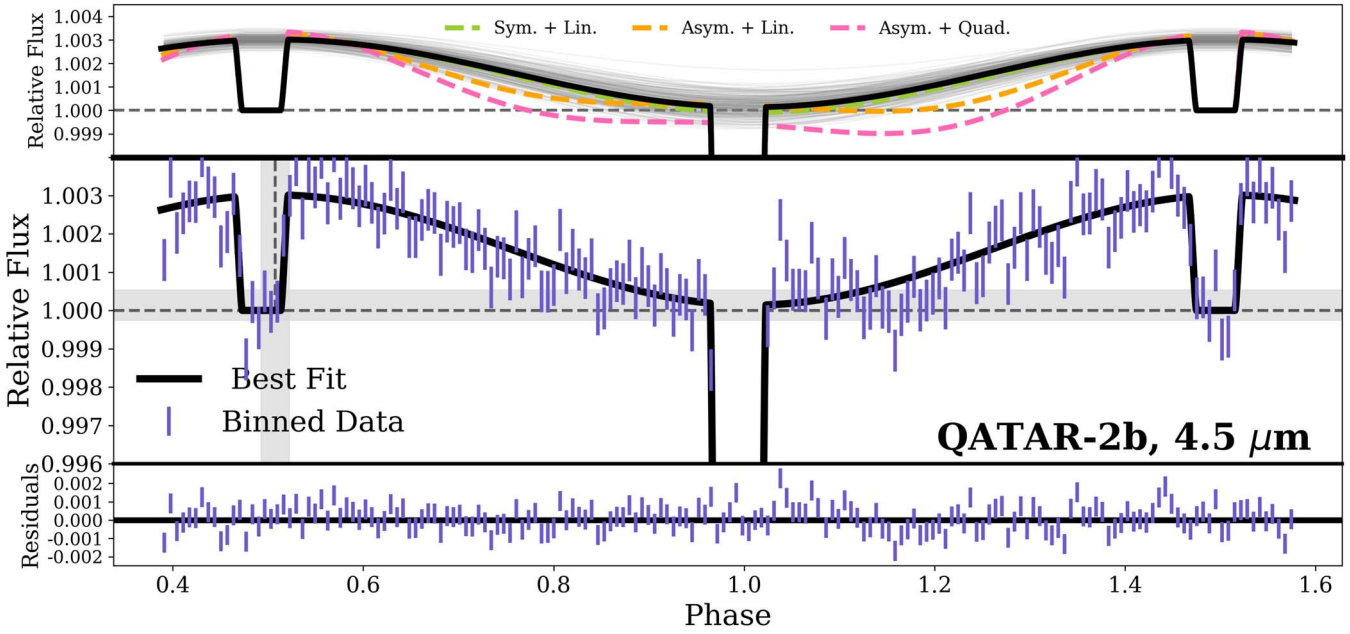

Figure 5. Qatar-2b 4.5 μm phase curve best fits. Top: best model combination (Symm. + Quad.) compared to the three other cases which result in a lower BIC but negative nightside fluxes. Two-hundred random draws of the best fit are shown as lightly shaded lines. Middle: best model compared to the binned data. The horizontal shaded regions correspond to the uncertainty on the minimum flux, while the vertical region corresponds to the uncertainty on the phase offset Bottom: the residuals.

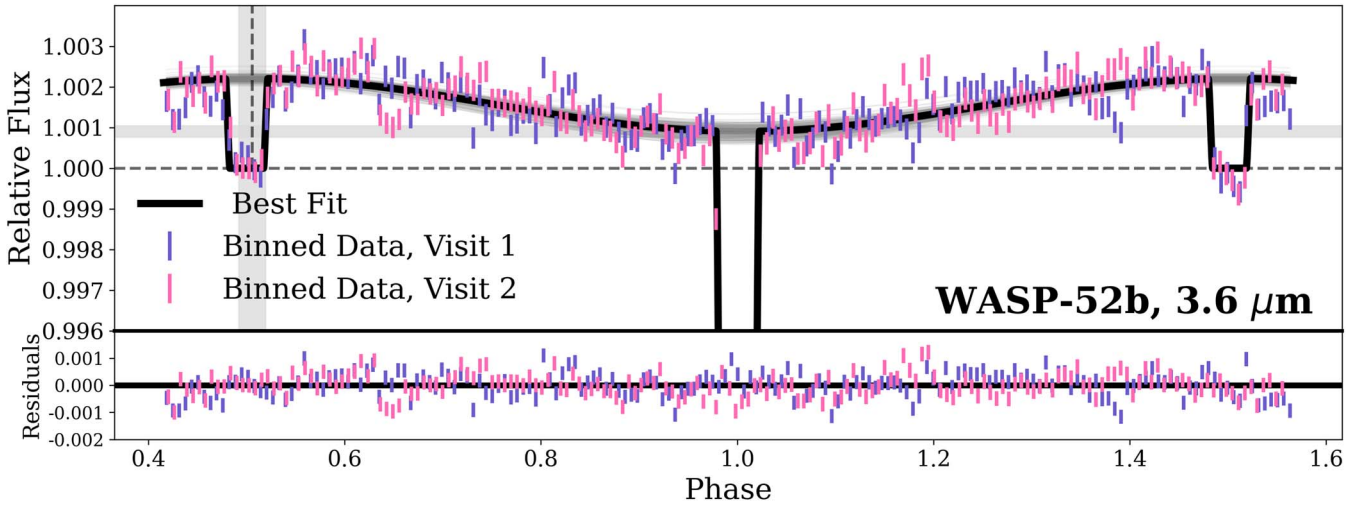

Figure 6. WASP-52b 3.6 μm phase curve best fit. Top: best model combination (Symm. + Lin.) compared to 200 random draws of the best fit, shown as lightly shaded lines. Binned data are overplotted. The horizontal shaded regions correspond to the uncertainty on the minimum flux, while the vertical region corresponds to the uncertainty on the phase offset. Bottom: the residuals.

All ramps with an asymmetric phase function place the hotspot squarely on the nightside of the planet with offsets 180°. With these offsets in strong disagreement with the measured 3.6 μm offset, we conclude that the fixed map is not appropriate for such strongly drifting centroids due to the secondary systematics this introduces. The middle panel of Figure 7 shows our best fit compared to the data, with residuals in the bottom panel.

For WASP-52b at 4.5 μm we measure a nightside band-integrated brightness temperature 1224 ± 77 K and a dayside band-integrated brightness temperature 1481 ± 34 K. Full results including amplitude, fluxes, offset, eclipse and transit depths are reported in Table 5. We caution that this data set is potentially unreliable and is worthy of follow-up with future missions.

4.4. WASP-34b

The 4.5 μm phase curve of WASP-34b is one of the longest phase curves observed by Spitzer, at 112.4 hours total over five AORs. As a result, there is a brief down-link gap after transit and an associated exponential ramp and large drifts in centroid position after WASP-34 was reacquired. Because the telescope had to move during the course of the phase curve, we fit the data before and after the gap with independent temporal ramps. In addition, the large drifts in centroid position associated with the start of the first AOR and the first AOR after the gap result in strong exponential trends in flux. These exponential changes in measured flux are poorly constrained by our fixed-sensitivity map, suggesting the instrument needed longer stabilization times both at the start of the observations and after the

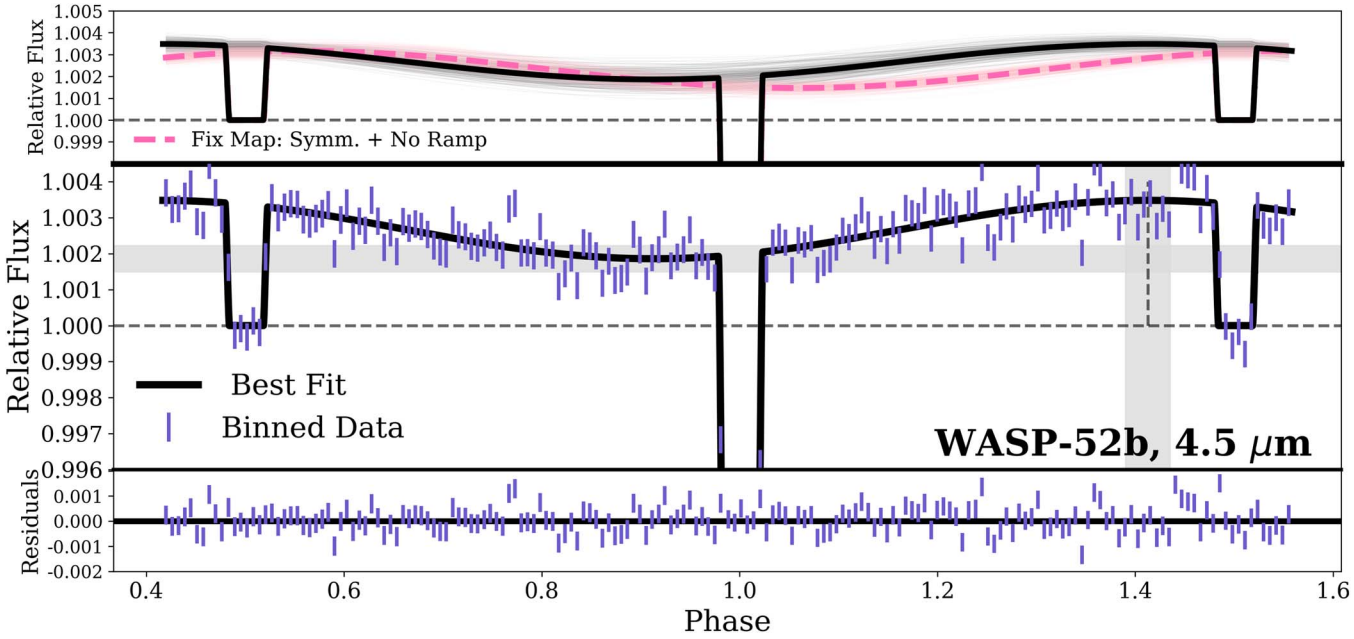

Figure 7. WASP-52b 4.5 μm phase curve best fit. Top: best model combination (Symm. + No Ramp) compared to 200 random draws of the best fit shown as lightly shaded lines in black. The fixed-map best fit is shown as a pink dashed line. Middle: best model compared to the binned data. The horizontal shaded regions correspond to the uncertainty on the minimum flux, while the vertical region corresponds to the uncertainty on the phase offset. Bottom: the residuals.

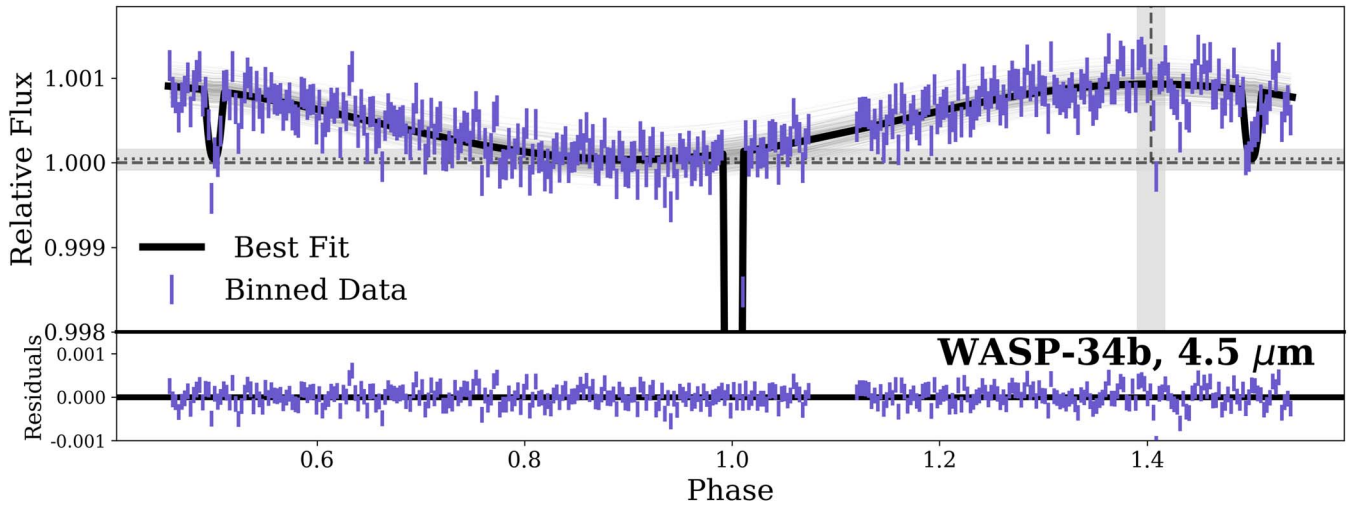

Figure 8. WASP-34b 4.5 μm phase curve best fit. Top: best model combination (Symm. + No Ramp) compared to 200 random draws of the best fit, shown as lightly shaded lines. Binned data are overplotted. The horizontal shaded regions correspond to the uncertainty on the minimum flux while the vertical region corresponds to the uncertainty on the phase offset. Bottom: the residuals. The dashed horizontal line denotes the stellar flux level and the dotted horizontal line denotes the in-eclipse flux, which is higher due to the grazing event. The gap around a phase of 1.1 is from a data down-link gap due to the 4.3 day orbital period.

down-link gap. Therefore, because of the unique situation this data gap causes, we do not apply the fixed-sensitivity map, and instead use standard BLISS mapping to self-calibrate the data.

For the two-component temporal ramp we test (1) an exponential + linear ramp combination to address the initial large drifts, (2) a linear ramp, and (3) no temporal ramp. For each case, the ramp is split into two components, before and after the down-link gap. The data is not well modeled with quadratic ramps. As highlighted in Table 4, we select "no ramp" as the best ramp model in combination with a symmetric phase function. Figure 8 shows our best-fit phase curve in combination with the binned data; residuals are shown in the bottom panel. Recall that the vertical shaded region shows the peak of the phase curve and associated uncertainty, while the horizontal shaded region corresponds to the uncertainty on the minimum of the phase curve.

To correct for the grazing event, we calculated the percentage of the planet that overlaps with the star, assuming an impact parameter of 0.904 from Smalley et al. (2011). We then renormalized the phase curve based on our calculated 47 ± 6 ppm contamination from the dayside of WASP-34b during eclipse. All reported values have been corrected for this.

Our best-fit results for WASP-34b at 4.5 μm give a nightside band-integrated brightness temperature 726 ± 119 K and a dayside band-integrated brightness temperature 1184 ± 47 K. Full results including amplitude, fluxes, offset, eclipse and transit depths are reported in Table 5. All values have been corrected to account for the grazing transit.

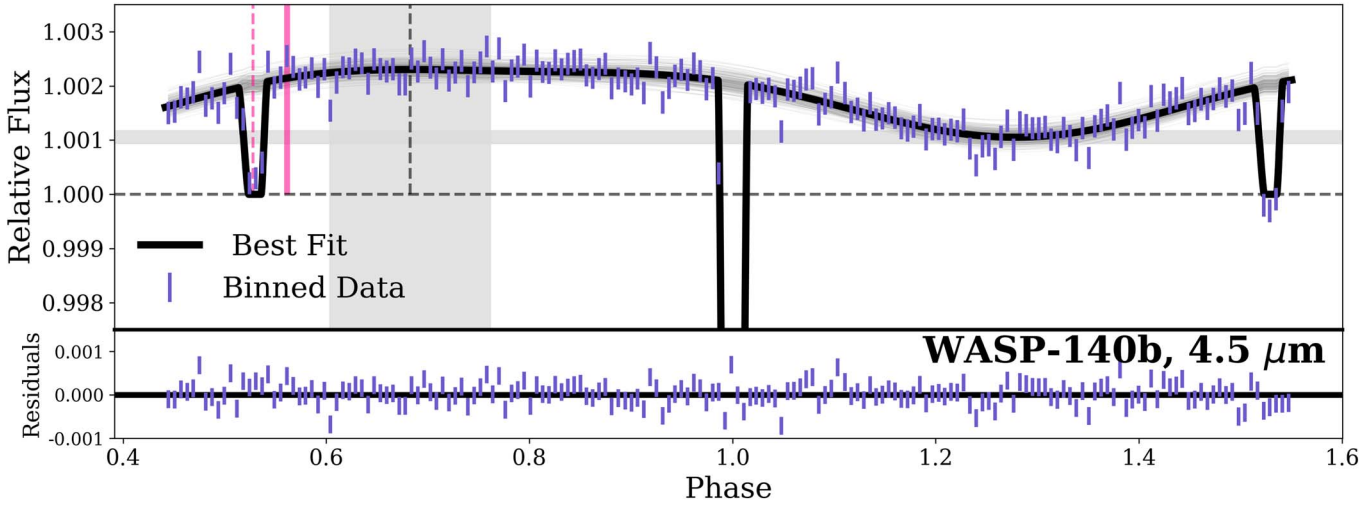

Figure 9. WASP-140b 4.5 μm phase curve best fit. Top: best model combination (Symm. + No Ramp) compared to 200 random draws of the best fit, shown as lightly shaded lines. Binned data are overplotted. The horizontal shaded regions correspond to the uncertainty on the minimum flux, while the vertical region corresponds to the uncertainty on the phase offset. Bottom: the residuals. As a reminder, WASP-140b has a slight eccentricity, possibly explaining the large westward offset. The solid pink line denotes periastron as compared to the secondary eclipse (dashed pink line).

4.5. WASP-140b

The 4.5 μm phase curve of WASP-140b was split into three AORs, each resulting in individual independent regions of centroids, as shown in Figures 1 and 2. As has been seen in other Spitzer data sets, independent groups of centroids result in stronger degeneracies between the systematic and astrophysical models. Luckily, each of the three groups of centroids at least partially overlaps with our fixed-sensitivity map, thus improving our ability to remove this degeneracy.

For comparison, we also fit the WASP-140b data set without our fixed-sensitivity map (i.e., using a standard BLISS approach). We found the results with a free map preferred flat (amplitude of zero) phase curves with longer than normal MCMC convergence times, suggesting the phase space of "allowed" fits is large. While typically our results both with and without our fixed-sensitivity map are similar in shape or general phase curve parameters, WASP-140b is a case in which an underlying phase curve could only be determined with the use of our fixed map. This is likely due to the three independent regions of centroids, which results in the phase function easily being modeled away by systematics.

Figure 9 shows our best fit compared to 200 random draws from the MCMC chains. Our best fit model for WASP-140b includes no temporal ramp and an asymmetric phase function with a large westward phase offset of $-55.^{\circ}7 \pm 28^{\circ}$.

Eastward offsets are expected for synchronously rotating hot Jupiters. However, a westward phase offset of $-23 \pm 4^{\circ}$ measured for CoRoT-2b (Dang et al. 2018) suggests that a large westward offset is not a newly observed or unique phenomenon. One possible explanation for WASP-140b's measured westward offset is that it is nonsynchronously rotating, which is supported by its eccentric orbit ($e = 0.047 \pm 0.0035$). Hellier et al. (2017) suggest that WASP-140b may have only recently arrived at its current, short-orbital-period location due to the system's short circularization time. Three-dimensional circulation models predict that such rotation rates (i.e., slower than synchronous) can shift the hotspot westward (e.g., Rauscher & Kempton 2014). While magnetic effects and deep jets can also produce westward-to-no phase offsets (e.g., Rogers & Komacek 2014; Carone et al. 2020), the equilibrium temperature of WASP-140b is below the threshold where magnetic effects are important. An additional explanation is that the peak of the phase curve simply corresponds to periastron passage, which occurs after secondary eclipse for WASP-140b, as denoted in Figure 9, affecting the shape and peak location of the observed phase curve (Lewis et al. 2010, 2013; Kataria et al. 2013; Mayorga et al. 2021, albeit for significantly higher eccentricities). Phase curves of the eccentric planets XO-3b ($e = 0.29$; Dang et al. 2022), WASP-14b ($e = 0.08$; Wong et al. 2015), and HAT-P-2b (e=0.51; Lewis et al. 2013) have also been observed by Spitzer. We leave a further discussion of the shape of the WASP-140b phase curve and its comparison to other eccentric planets for future work.

Our best-fit results for WASP-140b at 4.5 μm give a nightside band-integrated brightness temperature 1201 ± 29 K and a dayside band-integrated brightness temperature 1169 ± 25 K. Full results including amplitude, fluxes, offset, eclipse and transit depths are reported in Table 5. We note that the nightside (phase 0.0/1.0) appears warmer than the dayside (phase 0.5) because of the large phase offset.

5. Population Trends

Extracting robust population-level trends in hot Jupiters from Spitzer phase curve observations has proved difficult due to inconsistencies in data reduction and lack of consistent reporting of the phase curve and stellar parameters used to derive dayside and nightside temperatures, for example. This is commonly seen in large scatter in observed trends, as well as the disagreement between model trends and observed trends (see discussion in introduction). In this work we present a uniform sample for seven of the planets (the five from this work, as well as WASP-76b from May et al. 2021 and WASP-43b from May & Stevenson 2020) observed and analyzed as uniformly as possible, including adopting equilibrium temperatures calculated with the same stellar parameters used to convert planet–star flux ratios to brightness temperatures. This approach reduces potential bias as much as possible. The remainder of the population includes results from, in no particular order, HD 189733b (Knutson et al. 2012), HD

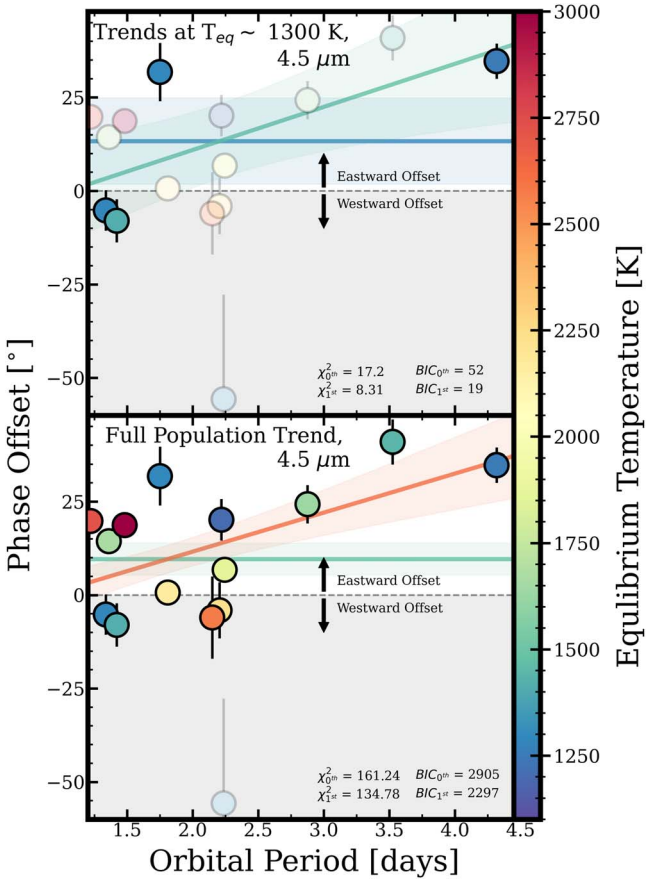

Figure 10. Phase offset at 4.5 μm vs. orbital period. Top: trend lines for $T_{eq} \sim 1300$ K sample only. Points outlined in black are the planets analyzed in this work (i.e., the 1300 K sample). The remaining sample is shown in the background. Bottom: trend lines for the complete sample of published hot Jupiter phase curves. For both panels, the color of each point corresponds to the equilibrium temperature. Overplotted are 1st-order and zeroth-order trend lines. In both cases we find the 1st-order linear trend best explains the observations.

209458b (Zellem et al. 2014), HAT-P-7b and WASP-19b (Wong et al. 2016), HD 149026b and WASP-33b (Zhang et al. 2018), WASP-18b (Maxted et al. 2013), WASP-12b (Bell et al. 2019), WASP-14b (Wong et al. 2015), WASP-103b (Kreidberg et al. 2018), KELT-16b and MASCARA-1b (Bell et al. 2021), and KEPT-9b (Mansfield et al. 2020). For these remaining planets in the Spitzer sample, it is not always clear what stellar and planetary parameters were used, so we adopt the equilibrium temperature reported in the composite parameters table of the NASA Exoplanet archive; exact parameters used can be found on our continuously updated repository of results (see link at the end of Section 1). Future work reanalyzing the literature sample will use consistent values.

Here we present evidence for a trend of increasing phase offset with orbital period at 4.5 μm, as shown in Parmentier & Crossfield (2018). In Figure 10 we show measured 4.5 μm hotspot offsets versus orbital period. The points outlined in black in the top panel are four of the five planets from this work, all with $T_{eq} \sim 1300$ K. WASP-140b is excluded from trend fitting due to its eccentric orbit and resulting anomalous offset. We find statistical evidence for an increasing trend of offset with period (ΔBIC $= -33$ as compared to just a flat line) for the remaining four planets in our $T_{eq} \sim 1300$ K sample (top), and when considering the entire set of literature values in addition to our new results (bottom) we find even stronger evidence for this linear trend of increasing offset with orbital period (ΔBIC $= -608$, as compared to just a flat line). We note, however, that this trend relies heavily on the three observed planets with orbital periods greater than 2.5 days.

The observational evidence for the existence of the offset versus orbital period trend is dynamically interesting because theory does not predict a dependence on rotation rate (which is related to orbital period for tidally locked planets). While Hammond & Pierrehumbert (2018) showed that the offset does depend on a nondimensional parameter, G, which is a function of scale height, gravity, radius, and rotation rate, it is not clear that rotation rate is the sole driver of that effect. In fact, Zhang & Showman (2017) predicted that the hotspot offset is solely driven by the ratio between the radiative and advective timescales. Because rotation rate should not affect the radiative timescale, the existence of this trend suggest that rotation rate has implications on the wind speed in tidally locked hot Jupiter atmospheres, namely that shorter-period (i.e., faster rotation rates) planets must have weaker equatorial jets. This trend can therefore be confirmed with ground-based, high-resolution spectroscopy that directly probes wind speeds in hot Jupiter atmospheres.

We also explore the potential for this trend of increasing phase offset with orbital period at 3.6 μm. The lack of reliable offset measurements past orbital periods of ~2.25 days at 3.6 μm precludes our ability to definitely detect such a trend specific to this channel; however, the measured offsets at 3.6 μm are statistically consistent with the 4.5 μm trend.

Additionally, we explore the relationship between the apparent heat redistribution $(T_b/T_{eq})^4$ versus the equilibrium temperature, as shown in Figure 11. This relationship between dayside brightness temperatures and the equilibrium temperature is dependent on the circulation efficiency and the planet's albedo, and has been predicted by Cowan & Agol (2011), Schwartz et al. (2017), and Parmentier et al. (2021). In Figure 11, we show the apparent heat-redistribution parameter at 4.5 μm versus the equilibrium temperature, compared to three secondary parameters denoted with color in the three panels. For the planets in our sample (darkly outlined points) we use the same stellar parameters to calculate the dayside brightness temperature and the equilibrium temperature for consistency (see Tables 2 and 3). However, because we do not know the stellar parameters used for most of the literature sample, there may be biases in the plotted literature (lightly outlined points) sample. We note that biases due to the unknown choice of stellar parameters in the literature are unlikely to explain all the scatter here due to that seen in our uniform sample alone.

Figure 11 shows lines corresponding to expected $(T_{day}/T_{eq})^4$ ratios for no heat redistribution (2.67), dayside-only redistribution (2.0), and full heat redistribution (1.0) from models, as well as trend lines from Parmentier et al. (2021) for bolometric and 4.5 μm expectations both with and without nightside clouds for $T_{eq} < 2000$ K. Because other three-dimensional models predict nightside clouds primarily dissipate above ~2000 K (e.g., Roman et al. 2021), we do not expect that a simple extrapolation of these trend lines to higher temperatures is appropriate, particularly because we would expect the cloudy and cloud-free models to converge (Roman et al. 2021). However, even with those caveats, we still see that approximately one-third of the literature sample fall above even the bolometric emission models

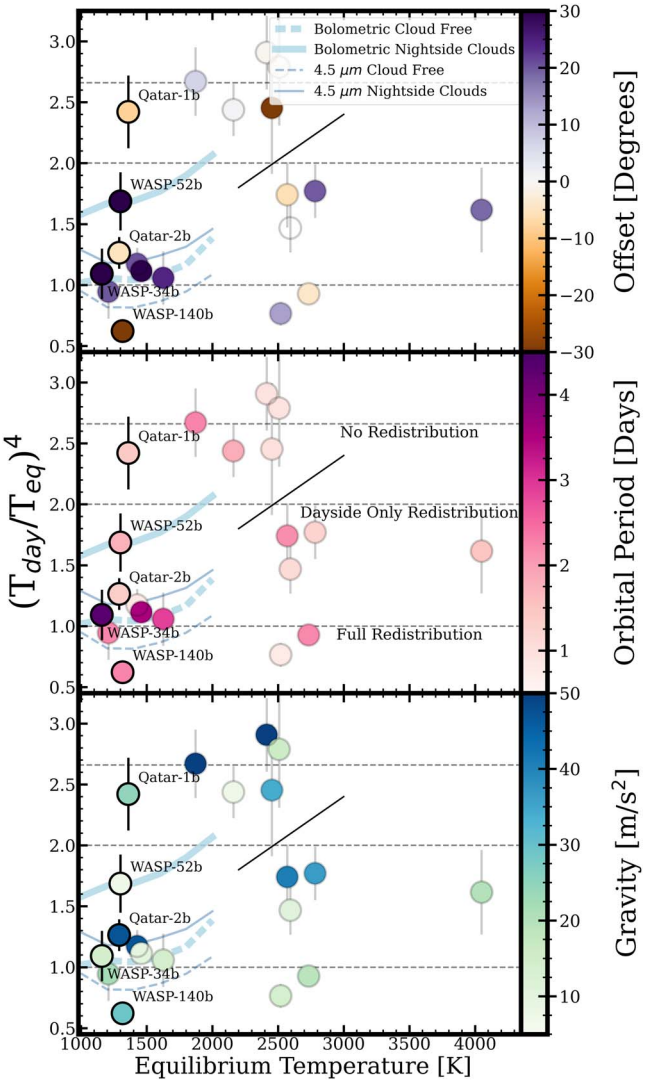

Figure 11. Apparent heat redistribution vs. equilibrium temperature compared to three different tertiary parameters: phase offset, orbital period, and gravity (shown with the color scales) for the 4.5 μm data. Models are from Parmentier et al. (2021) showing both 4.5 μm and bolometric emission (thin and thick lines, respectively) for both cloudy and clear (sold and dashed lines, respectively) cases. We note that some observations fall above even the bolometric predictions, suggesting a departure from current theory. Those points with dark outlines and error bars are our ∼1300 K sample. The remaining points are from literature values. From top to bottom, horizontal dashed lines denote values expected from no heat redistribution, dayside-only redistribution, and full redistribution. A solid line denotes an approximate division between literature planets with little heat distribution and those with a significant amount. There is no clear trend with offset, orbital period, or gravity.

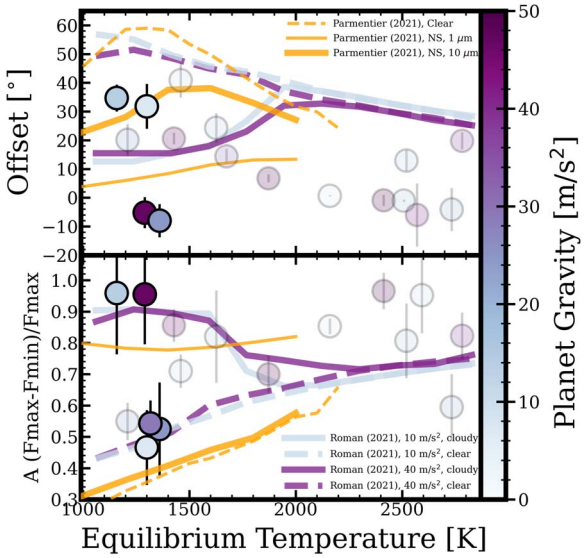

Figure 12. Offset and A_{obs} as a function of equilibrium temperature for the 4.5 μm data. It is not always clear if max and min or day and night (phase 1.0/0.5) values are reported in the literature, but we include all literature values here for completeness. Models are from Roman et al. (2021) and Parmentier et al. (2021). Our new ∼1300 K sample matches well with predicted trends from three-dimensional models. We identify a tentative trend of offset and gravity, which we explore more in Figure 13.

from Parmentier et al. (2021), suggesting even warmer daysides than expected from current theory. In our ∼1300 K sample, the hotter than expected dayside temperatures are further interesting due to their equilibrium temperature being below the threshold where MHD effects begin to affect the day–night heat transport (Menou 2012; Rogers & Komacek 2014; Hindle et al. 2021a, 2021b). As a result, unconsidered MHD effects cannot explain why Qatar-1b and WASP-52b have warmer than expected daysides compared to the Parmentier et al. (2021) models.

Importantly, we see a strong spread within our ∼1300 K sample (mean of $(T_b/T_{eq})^4 = 1.42$, with a standard deviation of 0.61), suggesting that secondary parameters are as important in predicting the heat transport efficiency in hot Jupiters as equilibrium temperature. We do not see any secondary trends in offset, orbital period (as a proxy for rotation rate, assuming tidally locked planets), or gravity, as shown in Figure 11.

We also explore previously predicted trends of offset and relative amplitude (here $(F_{max} - F_{min}) / F_{max}$) as a function of equilibrium temperature. Figure 12 shows the 4.5 μm data compared to three-dimensional model predictions from Roman et al. (2021) for both cloudy and clear cases at two different planetary gravities. While these models do use radiatively active clouds, which are important at cooler temperatures, we note that these do not consider magnetic drag (see, e.g., Rauscher & Menou 2013; Rogers & Komacek 2014; Rogers & Showman 2014; Beltz et al. 2022), which is likely to be important at high temperatures, nor H_2 dissociation or nongray impacts, all of which impact the hotspot offset and circulation (for the impact of the choice of radiative scheme on predicted phase curves, see, e.g., Lee et al. 2021). Nonequilibrium chemistry can also impact the emergent phase curve and is not considered in the model predictions we consider here (e.g., Steinrueck et al. 2019). We also compare to three-dimensional model predictions from Parmentier et al. (2021) for clear and two different nightside (labeled "NS") cloud particle sizes. We find good agreement between the Roman et al. (2021) model predictions and our observed amplitudes for our ∼1300 K sample, but a systematic offset toward smaller hotspot phase offsets for our sample compared to the literature values. However, the Parmentier et al. (2021) model offsets are a better match to our data. The large spread in model predictions highlights the numerous parameters than can impact the shape of hot Jupiter phase curves, as well as the different assumptions involved in these models.

In addition, there appears to be a slight relationship between gravity and offset seen in our ∼1300 K sample (the top panel). We explore this in Figure 13, where we consider trends within

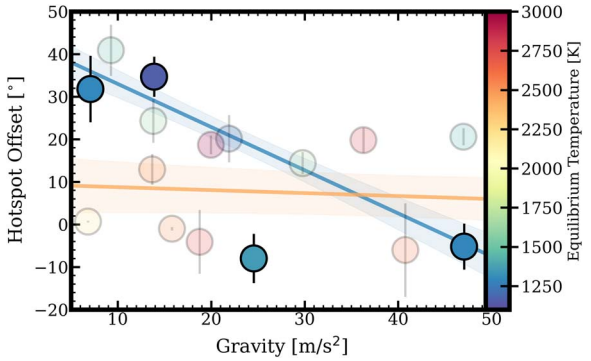

Figure 13. Hotspot offset vs. gravity, colored by equilibrium temperature, for the 4.5 μm data. Trend lines for our ∼1300 K sample (blue) and the remaining population (red) are shown. This suggests tentative evidence for a dependence off hotspot offset with gravity for cooler planets, which flattens off at higher equilibrium temperatures.

our sample and the remaining population (cool planets and warmer planets). There is evidence for a trend within our ∼1300 K sample of larger eastward offsets at low gravity, with slight westward offsets at high gravity, with this relationship flattening off for higher temperature planets. This may be expected due to, for example, magnetic drag in ultrahot planets resulting in no offset regardless of gravity. Further modeling including this effect may be useful to explore this trend more, particularly due to the apparent departure between the 10 m s^{-2} and 40 m s^{-2} case in the Roman et al. (2021) models in Figure 12.

Finally, our $T_{eq} \sim 1300$ K sample broadly agrees with previous observations that nightside temperatures of hot Jupiters are all approximately 1000 K (Beatty et al. 2019; Keating et al. 2019).

6. Conclusions

We have presented an analysis of seven new Spitzer phase curves and a reanalysis of one previously published phase curve. The five planets in our sample all have equilibrium temperatures of ∼1300 K. The analysis of these eight phase curves was performed as uniformly as the data allows with a goal of enabling comparative studies.

We identify a statistically significant trend of increasing phase curve hotspot offset with orbital period in both our 1300 K sample and the full Spitzer sample. Initial comparisons to models of apparent heat redistribution suggest there may be two populations of observed hot Jupiters with weak and strong redistribution, but a more uniform analysis is necessary to definitely make this assessment. We also identify tentative evidence of a hotspot offset dependence on gravity for cool planets. Our newly reduced sample agrees with expectations that planets of this equilibrium temperature should have fairly consistent nightside temperatures near ∼1000 K. Future work will reanalyze previous Spitzer phase curves with updated and uniform approaches to better understand the scatter in observed trends.

We also note that it may be informative to compare observational results to model-predicted trends in nondimensional units that incorporate a combination of parameters (e.g., the ratio of wave propagation and radiative timescales, the nondimensional Rossby deformation radius), but leave this to future work. With the continued reanalysis of Spitzer phase curves we will be able understand how multiple parameters (e.g., rotation rate/orbital period, gravity, equilibrium temperature, etc.) work together to shape the circulation of hot Jupiters, rather than single-parameter relationships.

This research has made use of the NASA Exoplanet Archive, which is operated by the California Institute of Technology, under contract with the National Aeronautics and Space Administration under the Exoplanet Exploration Program. This paper makes use of data from the first public release of the WASP data as provided by the WASP consortium and services at the NASA Exoplanet Archive.

E.M.M. acknowledges support from JHU APL's Independent Research And Development program and NASA XRP grant No. 80NSSC22K0313. K.B.S. and J.L.B. acknowledge support for this work from NASA through awards issued by JPL/Caltech (Spitzer programs 13038 and 14059). T.J.B. acknowledges support from the McGill Space Institute Graduate Fellowship, the Natural Sciences and Engineering Research Council of Canada's Postgraduate Scholarships-Doctoral Fellowship, and from the Fonds de recherche du Québec—Nature et technologies through the Centre de recherche en astrophysique du Québec. L.D. acknowledges support in part through the Technologies for Exo-Planetary Science (TEPS) PhD Fellowship, and the Natural Sciences and Engineering Research Council of Canada (NSERC)'s Postgraduate Scholarships-Doctoral Fellowship. J.M.D acknowledges support from the Amsterdam Academic Alliance (AAA) Program, and the European Research Council (ERC) European Union's Horizon 2020 research and innovation program (grant agreement no. 679633; Exo-Atmos). This work is part of the research program VIDI New Frontiers in Exoplanetary Climatology with project number 614.001.601, which is (partly) financed by the Dutch Research Council (NWO). M. M. was supported by NASA through the NASA Hubble Fellowship grant No. HST-HF2-51485.001-A awarded by the Space Telescope Science Institute, which is operated by the Association of Universities for Research in Astronomy, Inc. under NASA contract NAS 5-26555. Part of the research was carried out at the Jet Propulsion Laboratory, California Institute of Technology, under contract with the National Aeronautics and Space Administration

Software: Astropy (Astropy Collaboration et al. 2013, 2018), batman (Kreidberg 2015), ExoCTK (Bourque et al. 2021), IPython (Pérez & Granger 2007), Matplotlib (Hunter 2007), NumPy (van der Walt et al. 2011; Harris et al. 2020), SciPy (Virtanen et al. 2020).

Appendix
Fit Parameters

Table A1 lists the best-fit parameters and their uncertainties (if relevant) for all phase curves.

Table A1
Best-fit Parameters

Parameter	(Units)	qa001bo21	qa002bo11	qa002bo21	wa052bo11	wa052bo12	wa052bo21	wa034bo21	wa140bo21
Transit midpoint	BJD_{TDB}-2458000	242.0175 ± 0.000182	−95.9549 ± 9.4e-05	−103.9772 ± 0.000183	−320.0543 ± 0.000114	−320.0543 ± 0.000114	199.6311 ± 0.00014	762.307 ± 0.0002	486.4851 ± 0.000123
Rp/Rs	⋯	0.1451 ± 0.000823	0.1637 ± 0.000519	0.1619 ± 0.001007	0.1646 ± 0.000606	0.1646 ± 0.000606	0.163 ± 0.000721	0.1201 ± 0.001122	0.174 ± 0.000689
Period	Days	1.42	1.3371	1.3371	1.7498 ± 4e-06	1.7498 ± 4e-06	1.7498	4.3177	2.2369
a/Rs	⋯	6.247	5.96 ± 0.013589	5.9641 ± 0.021705	7.265 ± 0.010448	7.265 ± 0.010448	7.1989	10.6878 ± 0.028778	7.98
cos(i)	⋯	0.1031	0.0677	0.0677	0.0811	0.0811	0.0811	0.0837	0.1156
e	⋯	0.0	0.0	0.0	0.0	0.0	0.0	0.0	0.047
Ω	°	0.0	0.0	0.0	0.0	0.0	0.0	0.0	⋯4.0
u_1	(limb dark.)	0.101	0.1116	0.1	0.108	0.108	0.108	0.09	0.1
u_2	(limb dark.)	0.113	0.1166	0.125	0.147	0.147	0.147	0.099	0.125
Eclipse midpoint 1	BJD_{TDB}-2458000	241.3086 ± 0.001053	−96.6226 ± 0.000844	−104.6464 ± 0.0015	−320.9297 ± 0.001204	48.2759 ± 0.001246	198.7568 ± 0.000892	760.146 ± 0.00242	485.4285 ± 0.0028
T_{14}	Days	0.0672	0.0754	0.0754	0.0754	0.0754	0.0754	⋯	0.0631
Eclipse depth	ppm	2900.0 ± 161.0	2200.0 ± 118.0	3000.0 ± 185.0	2200.0 ± 77.0	2200.0 ± 77.0	3400.0 ± 162.0	⋯	2000.0 ± 111.0
T_{12}	Days	0.0142	0.0107	0.0107	0.0076	0.0076	0.0076	⋯	0.0223 ± 0.004917
T_{34}	Days	0.0142	0.0107	0.0107	0.0076	0.0076	0.0076	⋯	0.0135 ± 0.006333
Eclipse midpoint 2	BJD_{TDB}-2458000	242.7272 ± 0.001236	−95.2854 ± 0.001152	−103.3064 ± 0.001081	−319.1775 ± 0.000764	50.0266 ± 0.001014	200.5069 ± 0.000744	[a]	487.664 ± 0.003004
F_p/F_s [a]	ppm	⋯	⋯	⋯	⋯	⋯	⋯	800.0 ± 97.0	⋯
Full per. cos amp.	ppm	800.0 ± 144.0	1000.0 ± 141.0	1400.0 ± 184.0	600.0 ± 65.0	600.0 ± 65.0	800.0 ± 180.0	400.0 ± 41.0	600.0 ± 24.0
Full per. cos offset	Days	0.7601 ± 0.032978	0.7122 ± 0.021513	0.7101 ± 0.019904	0.8301 ± 0.023567	0.8301 ± 0.023567	0.852 ± 0.063766	2.0454 ± 0.05615	1.7087 ± 0.021923
Half per. cos amp.	ppm	⋯	⋯	⋯	⋯	⋯	⋯	⋯	200.0 ± 32.0
Half per. cos offset	Days	⋯	⋯	⋯	⋯	⋯	⋯	⋯	0.0607 ± 0.027693
Quadratic ramp term	⋯	−0.0019 ± 0.000485	−0.0026 ± 0.0006	0.0005 ± 0.000755	⋯	⋯	⋯	⋯	⋯
Linear ramp term	⋯	0.0024 ± 0.000241	0.0023 ± 0.000229	0.0012 ± 0.000226	0.0032 ± 7.9e-05	0.0187 ± 1.8e-05	⋯	⋯	⋯
Ramp offset	Days	0.0	0.0	0.0	0.0	4.0	⋯	⋯	⋯
PRF, Linear *X*	⋯	⋯	0.0683 ± 0.003633	−0.0009 ± 0.005045	−0.164 ± 0.005081	−0.007 ± 0.004743	0.0121 ± 0.005777	⋯	⋯
PRF, Quad. *X*	⋯	⋯	0.0572 ± 0.004632	0.2461 ± 0.057581	0.1696 ± 0.040813	−0.4528 ± 0.07063	0.0598 ± 0.035102	⋯	⋯

Table A1
(Continued)

Parameter	(Units)	qa001bo21	qa002bo11	qa002bo21	wa052bo11	wa052bo12	wa052bo21	wa034bo21	wa140bo21
PRF, Linear Y	⋯	⋯	-0.107 ± 0.004816	-0.2576 ± 0.016666	-0.1258 ± 0.007046	-0.0818 ± 0.006162	0.0336 ± 0.005722	⋯	⋯
PRF, Quad. Y	⋯	⋯	-0.1499 ± 0.051506	-2.5815 ± 0.134902	-1.34 ± 0.090374	0.3641 ± 0.029821	-0.2011 ± 0.033294	⋯	⋯
PRF offset	PRF-FWHM	⋯	0.6	0.6	0.6	0.6	0.6	⋯	⋯
Constant	Flux units	10716.2499 ± 1.117601	13813.3694 ± 6.325889	8547.7662 ± 4.977395	24419.5982 ± 1.055123	2977.2732 ± 2.310508	14058.807 ± 7.043908	49752.8256 ± 4.53561	34490.6782 ± 0.564251

Notes. Parameters in fits. Those without errors are held constant. All parameters have uniform priors that span the entire width of physically possible values.
[a] Due to the grazing nature of the WASPS-34b occultations we use a different functional form for the eclipses, as described in the text. This is a repeating function, so there is no second midpoint. The F_p/F_s term is also unique to this event and is comparable to the eclipse depth. The values for WASP-34b in this table are not corrected to account for the grazing event.

ORCID iDs

E. M. May https://orcid.org/0000-0002-2739-1465
K. B. Stevenson https://orcid.org/0000-0002-7352-7941
Jacob L. Bean https://orcid.org/0000-0003-4733-6532
Taylor J. Bell https://orcid.org/0000-0003-4177-2149
Nicolas B. Cowan https://orcid.org/0000-0001-6129-5699
Lisa Dang https://orcid.org/0000-0003-4987-6591
Jean-Michel Desert https://orcid.org/0000-0002-0875-8401
Jonathan J. Fortney https://orcid.org/0000-0002-9843-4354
Dylan Keating https://orcid.org/0000-0001-9887-4117
Eliza M.-R. Kempton https://orcid.org/0000-0002-1337-9051
Thaddeus D. Komacek https://orcid.org/0000-0002-9258-5311
Nikole K. Lewis https://orcid.org/0000-0002-8507-1304
Megan Mansfield https://orcid.org/0000-0003-4241-7413
Caroline Morley https://orcid.org/0000-0002-4404-0456
Vivien Parmentier https://orcid.org/0000-0001-9521-6258
Emily Rauscher https://orcid.org/0000-0003-3963-9672
Mark R. Swain https://orcid.org/0000-0002-0919-4468
Robert T. Zellem https://orcid.org/0000-0001-7547-0398

References

Alam, M. K., Nikolov, N., López-Morales, M., et al. 2018, AJ, 156, 298
Alsubai, K. A., Parley, N. R., Bramich, D. M., et al. 2011, MNRAS, 417, 709
Astropy Collaboration, Robitaille, T. P., Tollerud, E. J., et al. 2013, A&A, 558, A33
Astropy Collaboration, Price-Whelan, A. M., Sipőcz, B. M., et al. 2018, AJ, 156, 123
Ballard, S., Christiansen, J. L., Charbonneau, D., et al. 2010, ApJ, 716, 1047
Barnes, S. A. 2007, ApJ, 669, 1167
Baxter, C., Désert, J.-M., Tsai, S.-M., et al. 2021, A&A, 648, A127
Beatty, T. G., Marley, M. S., Gaudi, B. S., et al. 2019, AJ, 158, 166
Bell, T. J., Zhang, M., Cubillos, P. E., et al. 2019, MNRAS, 489, 1995
Bell, T. J., Dang, L., Cowan, N. B., et al. 2021, MNRAS, 504, 3316
Beltz, H., Rauscher, E., Roman, M., & Guilliat, A. 2022, AJ, 163, 35
Bourque, M., Espinoza, N., Filippazzo, J., et al. 2021, The Exoplanet Characterization Toolkit (ExoCTK), 1.0.0, Zenodo, doi: 10.5281/zenodo.4556063
Bryan, M. L., Alsubai, K. A., Latham, D. W., et al. 2012, ApJ, 750, 84
Campo, C. J., Harrington, J., Hardy, R. A., et al. 2011, ApJ, 727, 125
Carone, L., Baeyens, R., Mollière, P., et al. 2020, MNRAS, 496, 3582
Carter, J. A., & Winn, J. N. 2009, ApJ, 704, 51
Castelli, F., & Kurucz, R. L. 2003, in IAU Symp. 210, Modelling of Stellar Atmospheres, Poster Contributions (San Francisco, CA: ASP), A20
Charbonneau, D., Allen, L. E., Megeath, S. T., et al. 2005, ApJ, 626, 523
Collins, K. A., Kielkopf, J. F., & Stassun, K. G. 2017, AJ, 153, 78
Cowan, N. B., & Agol, E. 2008, ApJL, 678, L129
Cowan, N. B., & Agol, E. 2011, ApJ, 729, 54
Cowan, N. B., Machalek, P., Croll, B., et al. 2012, ApJ, 747, 82
Cubillos, P., Harrington, J., Madhusudhan, N., et al. 2013, ApJ, 768, 42
Dang, L., Cowan, N. B., Schwartz, J. C., et al. 2018, NatAs, 2, 220
Dang, L., Bell, T. J., Cowan, N. B., et al. 2022, AJ, 163, 32
Demory, B.-O., Gillon, M., Madhusudhan, N., & Queloz, D. 2016a, MNRAS, 455, 2018
Demory, B.-O., Gillon, M., de Wit, J., et al. 2016b, Natur, 532, 207
Fazio, G. G., Hora, J. L., Allen, L. E., et al. 2004, ApJS, 154, 10
Garhart, E., Deming, D., Mandell, A., Knutson, H., & Fortney, J. J. 2018, A&A, 610, A55
Garhart, E., Deming, D., Mandell, A., et al. 2020, AJ, 159, 137
Gillon, M., Demory, B. O., Lovis, C., et al. 2017, A&A, 601, A117
Hammond, M., & Pierrehumbert, R. T. 2018, ApJ, 869, 65
Harris, C. R., Millman, K. J., van der Walt, S. J., et al. 2020, Natur, 585, 357
Hébrard, G., Collier Cameron, A., Brown, D. J. A., et al. 2013, A&A, 549, A134
Hellier, C., Anderson, D. R., Collier Cameron, A., et al. 2017, MNRAS, 465, 3693
Helling, C., Gourbin, P., Woitke, P., & Parmentier, V. 2019, A&A, 626, A133
Hindle, A. W., Bushby, P. J., & Rogers, T. M. 2021a, ApJL, 916, L8
Hindle, A. W., Bushby, P. J., & Rogers, T. M. 2021b, ApJ, 922, 176
Hunter, J. D. 2007, CSE, 9, 90
Ingalls, J. G., Krick, J. E., Carey, S. J., et al. 2012, Proc. SPIE, 8442, 84421Y
Kataria, T., Showman, A. P., Lewis, N. K., et al. 2013, ApJ, 767, 76
Kataria, T., Sing, D. K., Lewis, N. K., et al. 2016, ApJ, 821, 9
Keating, D., Cowan, N. B., & Dang, L. 2019, NatAs, 3, 1092
Keating, D., Stevenson, K. B., Cowan, N. B., et al. 2020, AJ, 159, 225
Knutson, H. A., Charbonneau, D., Allen, L. E., Burrows, A., & Megeath, S. T. 2008, ApJ, 673, 526
Knutson, H. A., Charbonneau, D., Cowan, N. B., et al. 2009, ApJ, 703, 769
Knutson, H. A., Lewis, N., Fortney, J. J., et al. 2012, ApJ, 754, 22
Komacek, T. D., & Showman, A. P. 2016, ApJ, 821, 16
Komacek, T. D., Showman, A. P., & Tan, X. 2017, ApJ, 835, 198
Kreidberg, L. 2015, PASP, 127, 1161
Kreidberg, L., Line, M. R., Parmentier, V., et al. 2018, AJ, 156, 17
Krick, J. E., Ingalls, J., Carey, S., et al. 2016, ApJ, 824, 27
Lanotte, A. A., Gillon, M., Demory, B. O., et al. 2014, A&A, 572, A73
Lee, E. K. H., Parmentier, V., Hammond, M., et al. 2021, MNRAS, 506, 2695
Lewis, N. K., Showman, A. P., Fortney, J. J., et al. 2010, ApJ, 720, 344
Lewis, N. K., Knutson, H. A., Showman, A. P., et al. 2013, ApJ, 766, 95
Liddle, A. R. 2007, Mon. Not. R. Astron. Soc, 377, L74
Lust, N. B., Britt, D., Harrington, J., et al. 2014, PASP, 126, 1092
Mancini, L., Southworth, J., Ciceri, S., et al. 2014, MNRAS, 443, 2391
Mandel, K., & Agol, E. 2002, ApJL, 580, L171
Mansfield, M., Bean, J. L., Stevenson, K. B., et al. 2020, ApJL, 888, L15
Mansfield, M., Line, M. R., Bean, J. L., et al. 2021, NatAs, 5, 1224
Maxted, P. F. L., Anderson, D. R., Doyle, A. P., et al. 2013, MNRAS, 428, 2645
May, E. M., & Stevenson, K. B. 2020, AJ, 160, 140
May, E. M., Komacek, T. D., Stevenson, K. B., et al. 2021, AJ, 162, 158
Mayorga, L. C., Robinson, T. D., Marley, M. S., May, E. M., & Stevenson, K. B. 2021, ApJ, 915, 41
Mendonça, J. M., Malik, M., Demory, B.-O., & Heng, K. 2018, AJ, 155, 150
Menou, K. 2012, ApJ, 745, 138
Močnik, T., Southworth, J., & Hellier, C. 2017, MNRAS, 471, 394
Öztürk, O., & Erdem, A. 2019, MNRAS, 486, 2290
Parmentier, V., & Crossfield, I. J. M. 2018, Handbook of Exoplanets (Berlin: Springer), 116
Parmentier, V., Fortney, J. J., Showman, A. P., Morley, C., & Marley, M. S. 2016, ApJ, 828, 22
Parmentier, V., Showman, A. P., & Fortney, J. J. 2021, MNRAS, 501, 78
Pérez, F., & Granger, B. E. 2007, CSE, 9, 21
Perez-Becker, D., & Showman, A. P. 2013, ApJ, 776, 134
Perna, R., Heng, K., & Pont, F. 2012, ApJ, 751, 59
Rauscher, E., & Kempton, E. M. R. 2014, ApJ, 790, 79
Rauscher, E., & Menou, K. 2013, ApJ, 764, 103
Reach, W. T., Megeath, S. T., Cohen, M., et al. 2005, PASP, 117, 978
Rogers, T. M., & Komacek, T. D. 2014, ApJ, 794, 132
Rogers, T. M., & Showman, A. P. 2014, ApJL, 782, L4
Roman, M. T., Kempton, E. M. R., Rauscher, E., et al. 2021, ApJ, 908, 101
Schwartz, J. C., Kashner, Z., Jovmir, D., & Cowan, N. B. 2017, ApJ, 850, 154
Smalley, B., Anderson, D. R., Collier Cameron, A., et al. 2011, A&A, 526, A130
Stassun, K. G., Oelkers, R. J., Paegert, M., et al. 2019, AJ, 158, 138
Steinrueck, M. E., Parmentier, V., Showman, A. P., Lothringer, J. D., & Lupu, R. E. 2019, ApJ, 880, 14
Stevenson, K. B., Harrington, J., Fortney, J. J., et al. 2012, ApJ, 754, 136
Stevenson, K. B., Line, M. R., Bean, J. L., et al. 2017, AJ, 153, 68
ter Braak, C., & Vrugt, J. 2008, Stat. Comput., 18, 435
van der Walt, S., Colbert, S. C., & Varoquaux, G. 2011, CSE, 13, 22
Virtanen, P., Gommers, R., Oliphant, T. E., et al. 2020, NatMe, 17, 261
Wong, I., Knutson, H. A., Lewis, N. K., et al. 2015, ApJ, 811, 122
Wong, I., Knutson, H. A., Kataria, T., et al. 2016, ApJ, 823, 122
Zellem, R. T., Lewis, N. K., Knutson, H. A., et al. 2014, ApJ, 790, 53
Zhang, M., Knutson, H. A., Kataria, T., et al. 2018, AJ, 155, 83
Zhang, X., & Showman, A. P. 2017, ApJ, 836, 73